Anisotropic shear-wave velocity structure of the Earth's mantle: A global model

B. Kustowski,[1,2] G. Ekström,[3] and A. M. Dziewoński[1]

[1]   We combine a new, large data set of surface wave phase anomalies, long-period waveforms, and body wave travel times to construct a three-dimensional model of the anisotropic shear wave velocity in the Earth's mantle. Our modeling approach is improved and more comprehensive compared to our earlier studies and involves the development and implementation of a new spherically symmetric reference model, simultaneous inversion for velocity and anisotropy, as well as discontinuity topographies, and implementation of nonlinear crustal corrections for waveforms. A comparison of our new three-dimensional model, S362ANI, with two other models derived from comparable data sets but using different techniques reveals persistent features: (1) strong, ∼200-km-thick, high-velocity anomalies beneath cratons, likely representing the continental lithosphere, underlain by weaker, fast anomalies extending below 250 km, which may represent continental roots, (2) weak velocity heterogeneity between 250 and 400 km depths, (3) fast anomalies extending horizontally up to 2000–3000 km in the mantle transition zone beneath subduction zones, (4) lack of strong long-wavelength heterogeneity below 650 km suggesting inhibiting character of the upper mantle–lower mantle boundary, and (5) slow-velocity superplumes beneath the Pacific and Africa. The shear wave radial anisotropy is strongest at 120 km depth, in particular beneath the central Pacific. Lateral anisotropic variations appreciably improve the fit to data that are predominantly sensitive to the uppermost and lowermost mantle but not to the waveforms that control the transition zone and midmantle depths. Tradeoffs between lateral variations in velocity and anisotropy are negligible in the uppermost mantle but noticeable at the bottom of the mantle.

Citation: Kustowski, B., G. Ekström, and A. M. Dziewoński (2008), Anisotropic shear-wave velocity structure of the Earth's mantle: A global model, *J. Geophys. Res.*, *113*, B06306, doi:10.1029/2007JB005169.

1. Introduction

[2] Seismic tomography provides the most detailed view on the structure of the Earth's mantle. Consequently, a number of fundamental questions in solid Earth sciences have been addressed based on the interpretation of tomographic models. Differences between models are sometimes significant, however, and may lead to incompatible interpretations. Discrepancies between models may result from inaccurate measurements, insufficient data coverage, or different modeling techniques. The goals of this work are (1) building a new large set of data that constrains the structure of the mantle as uniformly as possible, (2) constructing a new three-dimensional (3-D) model of the mantle, and (3) the identification of features that are common to different well-constrained models obtained using different techniques.

[3] One of the problems addressed by seismic tomography is the determination of the thickness of the continental lithosphere. Early studies suggested that surface wave phase velocity variations could be explained by models with significant continent–ocean contrast confined to the region above 200 km depth [e.g., *Dziewonski*, 1971]. *Jordan* [1975], on the other hand, found indications that continental signatures may extend down to at least 400 km. Such thick continental roots may have survived without sinking or convecting disruption due to compositional buoyancy [*Jordan*, 1975, 1978, 1981] or high viscosity [*Shapiro et al.*, 1999]. Some recent models [*Mégnin and Romanowicz*, 2000; *Gu et al.*, 2001a] show the continental signatures extending below 300 km, while in others [*Masters et al.*, 2000; *Ritsema et al.*, 2004] strong continent–ocean differences are confined to the uppermost 200 km of the mantle. In this work, we investigate whether our new model, as well as other recent models [*Ritsema et al.*, 1999; *Panning and Romanowicz*, 2006] with significant sensitivity to the structures deeper than 200 km, still show significant discrepancies.

[4] The degree to which the convection in the upper mantle is separated from processes operating in the lower mantle is still a subject of debate. This issue is related, but

---

[1]Department of Earth and Planetary Sciences, Harvard University, Cambridge, Massachusetts, USA.

[2]Now at Chevron, San Ramon, California, USA.

[3]Lamont-Doherty Earth Observatory, Columbia University, Palisades, New York, USA.

not equivalent, to the question concerning the depth extent of subducted lithospheric slabs. Some tomographic models derived from travel times of body waves show narrow, high-velocity anomalies beneath major subduction zones extending down to midmantle depths or even to the lowermost mantle [e.g., *Grand et al.*, 1997; *van der Hilst et al.*, 1997]. These results are often taken as evidence for whole-mantle convection, but doubts have also been expressed regarding the resolving power of the travel time data used. *Boschi and Dziewonski* [1999], for example, showed that given the ray path coverage of teleseismic body waves, it is possible to obtain fictitious narrow slab-like anomalies even from the synthetic input data calculated without such structures. An alternative approach for studying the style of convection in the mantle involves using longer-period but diverse data sets recorded on broadband seismograms of the Global Seismographic Network (GSN) and Federation of Digital Broadband Seismic Networks (FDSN). These data allow for measuring various types of waves that together have significant sensitivity in all depth ranges in the mantle. Models of *Gu et al.* [2001a] and *Ritsema et al.* [2004], derived from diverse data sets, reveal a significant change in the heterogeneity at the upper mantle–lower mantle boundary, which may reflect a change in the flow pattern. Such interpretation is consistent with the observed depressions of this boundary [*Shearer and Masters*, 1992; *Flanagan and Shearer*, 1998; *Gu et al.*, 1998, 2003]. Since the style of convection still appears to be an unresolved problem, we reexamine the velocity heterogeneity and topography of the transition zone discontinuities and compare our results with other shear wave velocity models that constrain the transition region between the uppermost and lower mantle.

[5] Seismic tomography has also been used to map anisotropy in the lithosphere–asthenosphere system. Evidence for the presence of anisotropy in the upper mantle includes the discrepancy between models constrained by Rayleigh and Love waves, shear wave splitting, and azimuthal variations of P_n velocities (for review, see, for example, *Anderson* [1989]). The presence of anisotropy in the upper mantle is often explained in terms of lattice preferred orientation (LPO; for review, see *Nicolas and Christensen* [1987]) of anisotropic crystals, such as olivine, in the convecting asthenosphere, or a frozen-in anisotropy in the lithosphere. The shear wave anisotropy in PREM [*Dziewonski and Anderson*, 1981] is strongest at the Mohorovičić discontinuity (hereinafter referred to as Moho) and vanishes at the 220-km discontinuity, which was proposed to represent the base of a low-velocity zone and have the global extent [*Anderson*, 1979]. Three-dimensional models calculated as a perturbation with respect to PREM show very similar globally averaged anisotropy to the reference model [e.g., *Ekström and Dziewonski*, 1998; *Panning and Romanowicz*, 2006]. Since the 220-km discontinuity now appears not to have a global extent [e.g., *Gu et al.*, 2001b], it is desirable to investigate anisotropy in the uppermost mantle independently of PREM. *Boschi and Ekström* [2002] and *Nettles and Dziewoński* [2008] started their tomographic inversions using one-dimensional (1-D) isotropic models without the 220-km discontinuity. Their final models show depth variations of globally averaged anisotropic shear wave velocities that are significantly different than in PREM. However, these studies did not determine parame-

ters other than shear wave velocities as they considered only short- and intermediate-period surface waves in the inversion. Since our combined data set has a significant sensitivity to 1-D variations in all five elastic parameters of a radially anisotropic model, as well as the density, we develop a new 1-D model of the mantle describing variations in all these parameters. The model is then used as a reference in subsequent 3-D inversions.

[6] Surface wave data also require lateral variations of radial anisotropy in the upper mantle. *Ekström and Dziewonski* [1998] reported on a large region with anomalous anisotropy in the top 200 km of the mantle beneath the Pacific. *Panning and Romanowicz* [2006] also found a strong $v_{SH} > v_{SV}$ anomaly in the Pacific at 150 km, which, in contrast to the results of *Ekström and Dziewonski* [1998], does not change significantly at shallower depths. *Gung et al.* [2003] reported a strong $v_{SH} > v_{SV}$ trend not only in the suboceanic mantle but also beneath the continental lithosphere, and *Marone et al.* [2007] also found lateral variations in anisotropy under the North America. Significant anisotropic variations within continental plates were observed by *Nettles and Dziewoński* [2008]. *Zhou et al.* [2006] found $v_{SH} < v_{SV}$ anomalies beneath the Mid-Atlantic Ridge and the Red Sea extending at least to a depth of 400 km, and *Gu et al.* [2005] and *Panning and Romanowicz* [2006] reported deep anisotropy beneath the East Pacific Rise. Given the discrepancies between different models, we find it useful to search for robust lateral anisotropic variations in the most recent models with good global data coverage in the whole mantle.

[7] Finally, we investigate the anisotropy below the lithosphere–asthenosphere system. The presence of the anisotropic post-Perovskite phase in the lowermost mantle has been suggested by experimental results [*Murakami et al.*, 2004; *Oganov and Ono*, 2004; *Shim et al.*, 2004]. Regional seismic studies [*Vinnik et al.*, 1989; *Lay et al.*, 1998; *Kendall*, 2000] show significant anisotropy in the D'' region, which might be explained in terms of LPO, horizontal layering, or aligned inclusions [*Kendall and Silver*, 1996; *Karato*, 1998]. *Panning and Romanowicz* [2006] made the first attempt to map the anisotropy in the whole mantle on a global scale using nonlinear asymptotic coupling theory (NACT) [*Li and Romanowicz*, 1996] and reported the presence of significant anisotropic variations both in the D'' region and in the transition zone. In particular, they attributed the predominantly $v_{SH} > v_{SV}$ anisotropy in the lowermost mantle to horizontal flow and deviations from this pattern to upwellings at superplumes. In this work, we investigate whether anisotropy in these depth ranges is required by teleseismic body wave travel times and seismograms inverted using the path average approximation. We also test how velocity–anisotropy trade-offs affect the anisotropic variations.

[8] Thirty years after the first global tomographic model of the mantle was published [*Dziewonski et al.*, 1977], it is interesting to ask what tomographers have been trying to accomplish and which features of tomographic models have turned out to be robust. It has been tempting for many researchers to look for small-scale structures in the mantle; however, using more free parameters in the inversion does not necessarily lead to models with higher resolution [*Boschi and Dziewonski*, 1999]. Given limited and noneven

Table 1. Data Used in This Study[a]

Data	
	Number of surface wave phase anomalies
Love waves T = 35–150 s	55,510–83,904
Rayleigh waves T = 35–150 s	160,470–206,560
	Number of long-period waveforms
Body waves T >50 s	19,117–22,522
Mantle waves T >125 s	16,440–24,101
Mantle waves T >200 s	939–1,062
	Number of body wave travel times
S (HRV)	27,660
SS (HRV)	11,695
ScS (HRV)	4,397
ScSScS (HRV)	1,279
SS-S (HRV)	5,671
ScS-S (HRV)	3,471
S-SKS (HRV)	3,671
SKKS-SKS (HRV)	2,232
SS-S (SC)	16,180
ScS-S (SC)	7,902
SS-S410S (HRV)	18,677
SS-S650S (HRV)	18,670
S410S-S650S (HRV)	16,957

[a]Phase anomalies of surface waves are measured at nine periods using the same method as in the work of *Ekström et al.* [1997] but the data set has been extended compared to the original paper. We use seismograms from the years 1994–2003 to build a new set of 219 well-recorded $6.5 \leq M_w < 8$ earthquakes and 10 great ($M_w \geq 8$) earthquakes. For the great earthquakes we analyzed mantle waves with T > 200 s, and for smaller events we included mantle waves with T > 125 s and body waves with T > 50 s. Body wave travel times indicated by HRV were measured at Harvard and those indicated by SC were measured at Scripps. In the right column, we show the ranges of the number of surface wave phase anomaly measurements at different periods; the ranges for the number of waveforms measured on the vertical, longitudinal, and transverse components; and the number of different travel time measurements.

data coverage, typical for mantle tomography, some features of overparameterized models may strongly depend on regularization. Longer-wavelength anomalies can more easily be constrained and they tend to be independent of the modeling technique, as we demonstrate in this paper. Notably, the similarity between models discussed here is higher compared to earlier tomographic models. The improved consistency between the models has to be, at least in part, attributed to the completeness of the data used in the inversions. Therefore it is instructive to first review the data that constrain the velocity structure in different regions of the mantle.

2. Data Sets and Sensitivity Kernels

[9] In order to constrain the structure at all depths in the mantle, we combine three different types of data shown in Table 1, which we discuss throughout this section. According to ray theory, travel times of teleseismic body waves have a peak sensitivity at the turning point of the ray in the lower mantle but they sample the upper mantle only beneath the sources, receivers, and points of surface reflection. The structure of the uppermost mantle is very well constrained by the measurements of fundamental-mode surface waves, which, however, have little sensitivity at depths larger than 300 km. The transition zone is best sampled by overtone data, which are included in this work through the waveform inversion. *Ritsema et al.* [2004] demonstrated that when only one out of the three types of data is used, the resulting tomographic model will be well constrained only in a

limited range of depths and therefore will not reflect the overall structure of the mantle. While inversions of diverse data sets have been performed before [e.g., *Dziewonski and Woodward*, 1992; *Masters et al.*, 2000; *Gu et al.*, 2001a], our new data set is significantly larger compared to earlier models obtained at Harvard.

[10] In this section, we present our new data and methods used to determine their sensitivity to the radially anisotropic velocity structure. We analyze all our data using ray theory, which is computationally efficient and therefore suitable for combining large and diverse data sets. More complex approximations have been developed and implemented for certain types of data [e.g., *Montelli et al.*, 2004a, 2004b]. These methods, however, do not allow for as efficient computation of the sensitivity kernels as ray theory. The choice of theoretical approximations affects tomographic models less than data coverage and choices of parameterization and regularization schemes, as pointed out by *van der Hilst and de Hoop* [2005]. For the case of surface wave tomography, *Trampert and Spetzler* [2006] show that models obtained with one theory can be obtained using the other one by adjusting the regularization of the inverse problem. For the case of body wave tomography, the differences between the two models obtained with ray theory and finite-frequency (FF) theory presented by *Montelli et al.* [2004b] are significantly smaller than those among models compared by *Boschi and Dziewonski* [1999] using the same theory and data but different parameterization and damping. While developing more sophisticated theories may prove useful in the future, we believe that at this point, significant progress in understanding the overall structure of the mantle can be achieved by combining data that sample the mantle as uniformly as possible and experimenting with the model parameterization and regularization.

[11] Although all recorded seismic waves sample the Earth's crust, our long-period data cannot resolve details of the crustal structure. We assume that crustal effects can be accounted for by subtracting the predictions of a detailed global model CRUST2.0 of *Bassin et al.* [2000] from the data.

2.1. Surface Wave Dispersion

[12] The sensitivity of a surface wave to the Earth's structure is approximately constant along the ray path. Owing to this property and excellent ray path coverage, surface waves provide the best constraints on the lateral heterogeneity in the uppermost mantle. Surface waves of different frequencies sample different depth ranges and measurements of dispersion can therefore resolve vertical variations in the velocity structure. In this work, we employ fundamental-mode Rayleigh and Love waves measured at nine periods between 35 and 150 s. The phase anomalies have been collected by the seismology group at Harvard from seismograms recorded on the GSN and FDSN stations in the years 1992–2001. The measurement technique is the same as in the work of *Ekström et al.* [1997]. Extending the phase anomaly data set compared to the original paper increased the number of observations by a factor of four for Love waves and five for Rayleigh waves. At each period we have measured phases of each wave for more than 55,000 paths (Table 1). For comparison, the work of *Panning and Romanowicz* [2006] involves ∼16,000–
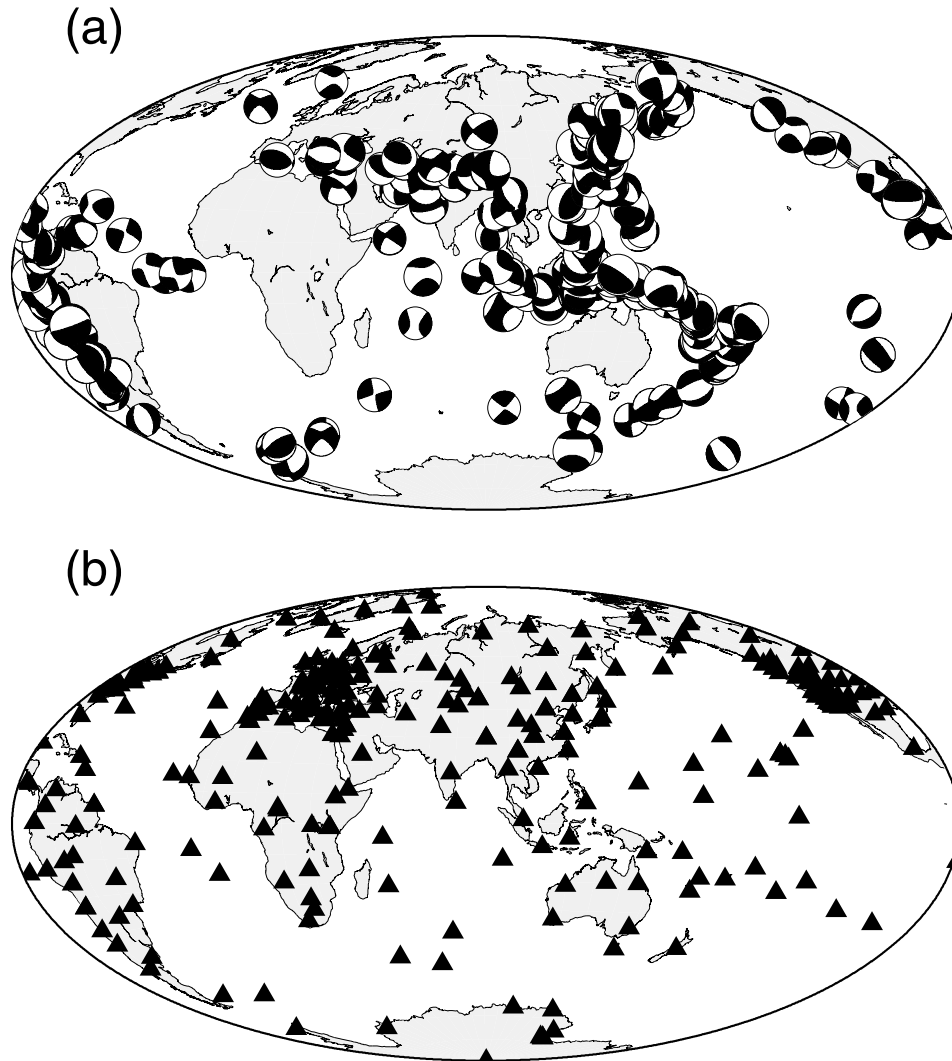
(a)

(b)

Figure 1. (a) Our new waveform data set consists of 219 earthquakes of $6.5 \leq M_w < 8$ and 10 earthquakes of $M_w \geq 8$ from the years 1994–2003. Harvard CMT solutions for these events are shown as "beach balls." (b) The distribution of all 320 broadband seismic stations of the Global Seismographic Network and Federation of Digital Broadband Seismic Networks used in this study.

36,000 wave packets recorded at different components, and *Zhou et al.* [2006] used a total of ~12,000 wave trains.

[13] Owing to the expansion of the data set, more than 200 rays hit every 1000-by-1000-km region on the Earth's surface, even for the smallest subsets of data. The nominal lateral resolution of our model is of the order of 1000 km. In the depth range controlled by surface waves, the lateral heterogeneity in our model is therefore almost insensitive to the regularization of the inverse problem.

[14] To find the relationship between the observed phase anomalies $\delta\Phi$ and the Earth's structure, we follow *Ekström* [2000] and write

$$\delta\Phi = -\frac{\omega}{c_0} \int_{path} \frac{\delta c}{c_0} \, ds, \qquad (1)$$

where δc is the local phase velocity anomaly, and c_0 is the phase velocity of the reference model. The phase velocity perturbation at a fixed frequency ω is related to the

frequency perturbation at a fixed wave number k [*Dahlen and Tromp*, 1998] by $(\frac{\delta c}{c})_\omega = \frac{c}{U}(\frac{\delta\omega}{\omega})_k$, where U is the group velocity. We define the perturbation in normal-mode eigenfrequency as

$$\delta\omega = \int_0^a \sum_{i=1}^6 \delta m_i K_{m_i} \, dr + K_{410}\delta h_{410} + K_{650}\delta h_{650}, \qquad (2)$$

where the integral is taken over the radius r from the Earth's center to the free surface at $a = 6371$ km, and m_i stands for the five parameters defining the transversely isotropic medium v_{PH}, v_{PV}, v_{SH}, v_{SV}, and η, as well as the density ρ. Fréchet kernels, or partial derivatives of the angular frequency ω with respect to m_i, are indicated by K_{m_i}, and the derivatives with respect to the changes in depth of the discontinuities δh_{410} and δh_{650} by K_{410} and K_{650}. All partial derivatives are calculated from eigenfunctions of normal modes in the spherically symmetric Earth model [*Takeuchi and Saito*, 1972; *Dahlen and Tromp*, 1998].

2.2. Mantle and Body Wave Waveforms

[15] We use seismograms from the years 1994–2003 to build a new set of 219 well-recorded $6.5 \leq M_w < 8$ earthquakes and 10 great ($M_w \geq 8$) earthquakes (Figure 1a). For the great earthquakes we analyzed only very-long-period waves with $T > 200$ s. Figure 1b shows the distribution of the GSN and FDSN stations used in this study. Compared to previous tomographic models developed at Harvard [*Gu et al.*, 2001a, 2003], we have increased the number of waveforms by a factor of 3.5 to 12 for different types of waves, and an additional data set has been created from very-long-period seismograms recorded for 10 great earthquakes, which further improve the sensitivity to the structure of the transition zone and the uppermost lower mantle. To ensure good global coverage, we select earthquakes that have occurred over 10 years, and to decrease computational time, we divide the Earth into approximately equal area 4-by-4-degree regions and typically select only the best-recorded event in each region. We allow two earthquakes in a region if they provide significantly different information about the Earth's structure due to different magnitudes or focal depths.

[16] The waveforms are inverted for the Earth's structure using the path average approximation [*Woodhouse and Dziewonski*, 1984]. The synthetic seismograms are constructed by the superposition of normal modes of the Earth and the sensitivity of mode eigenfrequency to the Earth's structure is defined by equation (2). The calculation of synthetic seismograms is improved by the implementation of nonlinear crustal corrections, which account for nonlinear effects on normal-mode eigenfrequency, and are discussed in detail by *Kustowski et al.* [2007].

[17] *Li and Romanowicz* [1995] showed that the path average approximation and the NACT retrieve nearly identical patterns of shear wave velocities but the anomalies that they obtained using the path average approximation appeared to be dramatically underestimated in the lower mantle. However, *Su and Dziewonski* [1991] gave the lower mantle-sensitive portions of seismograms high weights in the inversion and obtained a model with reasonably strong anomalies in the lower mantle. That is, both the strength and lateral variations of the SS travel time residuals predicted by this model are consistent with the observed ones.

[18] In our model, the lower mantle is constrained not only by the body wave waveforms but also by the arrival times of body waves. The amplitudes of the anomalies should therefore be properly resolved even if the lower-mantle-sensitive portions of seismograms were not strongly weighted in the inversion.

2.3. Body Wave Travel Times

[19] The structure of the lower mantle and the topographies of the transition zone discontinuities are constrained in this work predominantly by three sets of arrival times of teleseismic body waves measured at a dominating period of ~20 s (Table 1). The first arrival time data set was collected at Harvard by *Liu and Dziewonski* [1998] and consists of travel time residuals obtained by cross-correlation of observed and synthetic seismograms. The second data set, collected at Scripps by *Woodward and Masters* [1991] and *Bolton and Masters* [2001], consists of ScS−S and SS−S travel times measured through cross-correlation of the observed ScS, or the Hilbert transformed SS waveform, with the S-wave portion of the seismogram. In addition, the Scripps data require the correction for differential attenuation of SS and S waveforms. The Scripps data set contains many more ScS−S and SS−S travel times than the Harvard one but does not contain data for many of the phases measured at Harvard. Because Harvard and Scripps data have been measured using different techniques, we investigate their consistency before inverting them jointly for mantle velocity structure. We compare the two data sets by plotting the SS−S residuals with respect to PREM. The residuals are averaged at the surface bounce point of SS or core bounce point of ScS in 2-by-2-degree cells. When all data are plotted (Figure 2a), it is evident that the measurements from Scripps improve the data coverage, but it is not clear whether the data measured by two groups are consistent with each other. When we select only those ray paths that have similar locations of sources and receivers in both data sets, the overlapping subsets are very consistent with each other (Figure 2b) suggesting that the differences observed in Figure 2a result primarily from different ray path coverage. The two ScS−S data sets are also consistent with each other (Figure 2c). Some times measured at Scripps differ from those measured at Harvard by several seconds; however, they are rare and therefore not likely to significantly affect the inversion.

[20] Despite the similarity of the lateral variations, the average SS−S residual measured at Scripps is smaller by ~2 s than that of Harvard, and by ~1.1 s when only overlapping subsets are considered. Since the baseline shift is not observed for the ScS−S data, we attribute the shift to the SS bounce point, which requires the Scripps SS waveforms to be Hilbert transformed and corrected for differential attenuation, whereas the Harvard data do not require such procedure. Since no curvature is observed in the scatter plot (Figure 2c), we simply add a constant correction of 1.1 s to the SS−S data measured at Scripps prior to inversions. Adding the constant does not affect lateral velocity variations but it might change the global average. However, we do not allow the travel-time data to control the lower mantle in our new 1-D reference model; the model is forced to converge to PREM at 1320 km depth.

[21] The variance estimated for rays traveling along similar paths is nearly identical for the Harvard and Scripps data [*Kustowski*, 2007]. This suggests similar quality of the two data sets, which, in conjunction with the consistency of the lateral variations, and nonoverlapping ray path coverage, justifies combining the two data sets.

[22] The third data set consists of SS-S_{410}S, SS-S_{650}S, and S_{410}S-S_{650}S differential travel times measured by *Gu and Dziewonski* [2002] and *Gu et al.* [2003]. This data set provides evenly distributed constraints on the topography of the transition zone discontinuities. Following *Gu et al.* [2003], we invert simultaneously for mantle velocities and topographies of the discontinuities. The general form of the equation governing the inversion of travel time anomalies δt can be written as

$$\delta t = -\int_{path} \frac{\sum_{i=1}^{5} \delta m_i T_{m_i}}{\left(v_0^{group}\right)^2} ds + \sum_{d_{410}} T_{410}\, \delta h_{410} + \sum_{d_{650}} T_{650} \delta h_{650}, \quad (3)$$
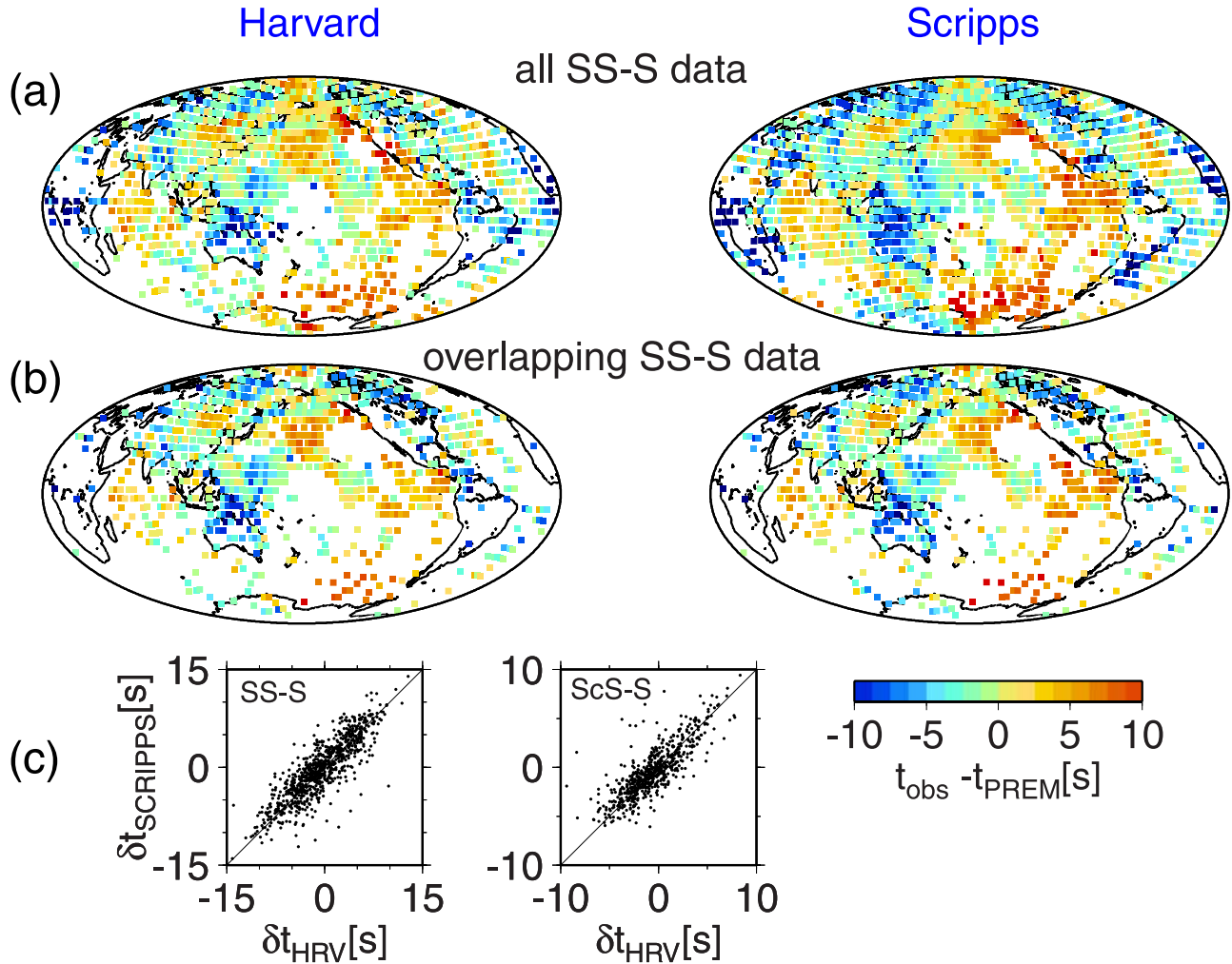
Figure 2. Travel-time residuals averaged in 2-by-2-degree cells, plotted at the midpoint between the source and receiver if at least one observation is available in the cell. (a) All SS-S data. (b) Only those SS-S ray paths that have similar locations of sources and receivers in both data sets. (c) Scatterplots for SS-S residuals from Figure 2b and for the overlapping ScS−S data from Harvard (HRV) and Scripps. The SS-S and ScS-S residuals are correlated at 0.86 and 0.82 level, respectively. A baseline shift of 1.1 s was added to the SS−S residuals measured at Scripps in Figures 2a, 2b, and 2c, as discussed in the text. All residuals are corrected for the effects of CRUST2.0 and Earth's ellipticity.

where d_{410} and d_{650} indicate all interactions of the ray with the discontinuities, and m_i stands for v_{PH}, v_{PV}, v_{SH}, v_{SV}, and η. Sensitivities T_{410} and T_{650} to the depth perturbations δh_{410} and δh_{650} are, for example, in the work of *Dziewonski and Gilbert* [1976]. We determine ray paths through the reference model using formulas of *Woodhouse* [1981] and calculate partial derivatives T_{m_i} and group velocities v_0^{group} based on ray theory for the transversely isotropic medium, as described in Appendix A.

3. New 1-D Reference Earth Model

3.1. Parameterization and Inversion

[23] The starting model used in the inversion for our new 1-D reference model is identical to PREM at crustal depths, between 220 and 400 km, and below 670 km. Between the Moho and 220 km depth, the model is isotropic and obtained by linearly extrapolating the elastic structure from below the 220 km depth, as in the work of *Boschi and*

Ekström [2002] and *Nettles and Dziewoński* [2008]. We fix the boundaries of the transition zone at 410 and 650 km. These depths are consistent with the most uniform constraints available on topography of these discontinuities [*Gu et al.*, 2003]. *Flanagan and Shearer* [1998], however, estimate the mean depths of these discontinuities to be 418 and 660 km, respectively. We remove a second-order discontinuity defined in PREM at 600 km depth. We take the attenuation structure from the model QL6 [*Durek and Ekström*, 1996], which fits surface wave and normal-mode data better than PREM. To account for changes with respect to PREM near 400, 600, and 670 km depths, we use linear extrapolation.

[24] We parameterize the model in terms of approximately isotropic variations

$$\frac{\delta v_S}{v_S^0} = \frac{\frac{\delta v_{SH}}{v_{SH}^0} + \frac{\delta v_{SV}}{v_{SV}^0}}{2} \quad \text{and} \quad \frac{\delta v_P}{v_P^0} = \frac{\frac{\delta v_{PH}}{v_{PH}^0} + \frac{\delta v_{PV}}{v_{PV}^0}}{2}, \qquad (4)$$
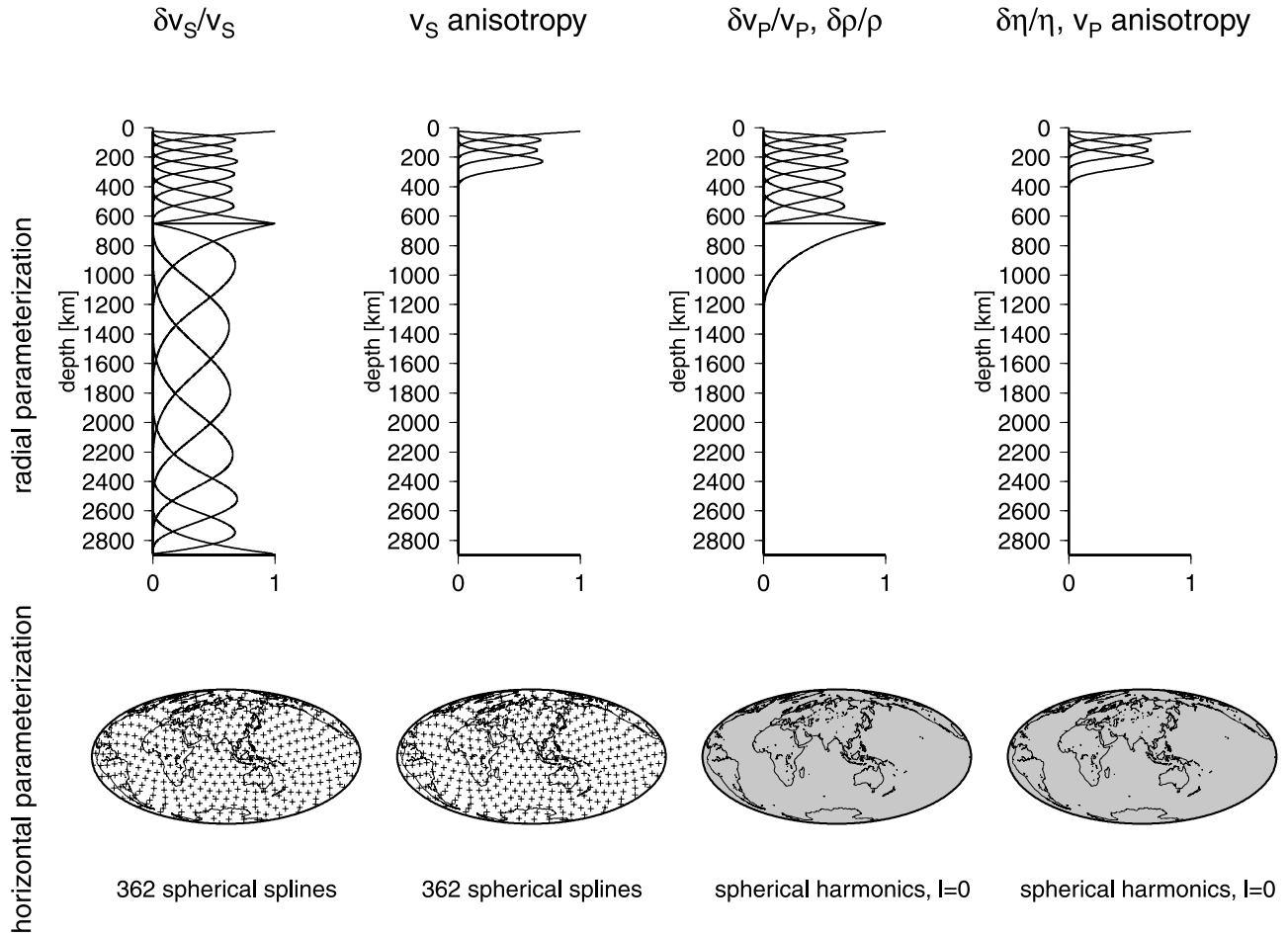
Figure 3. Three-dimensional parameterization of the mantle used in the derivation of the new reference model STW105. At each iteration, a new model is calculated as a spherical average of a three-dimensional perturbation with respect to the previous model. Pluses indicate knots of 362 spherical splines used to describe lateral variations in shear wave velocity and anisotropy. Degree-zero spherical harmonics represent perturbations in compressional-wave velocity and anisotropy, η, and density. The number of cubic splines used to describe vertical variations varies between 4 and 16 for different parameters.

and anisotropic variations

$$\frac{\delta a_S}{a_S^0} = \frac{\delta v_{SH}}{v_{SH}^0} - \frac{\delta v_{SV}}{v_{SV}^0} \text{ and } \frac{\delta a_P}{a_P^0} = \frac{\delta v_{PH}}{v_{PH}^0} - \frac{\delta v_{PV}}{v_{PV}^0}, \qquad (5)$$

where the superscript "0" indicates the reference model from previous iteration, and a denotes a measure of anisotropy. However, we always convert the arithmetic average into the Voigt average before plotting our models. Variations $\delta v_{SH}/v_{SH}^0$, $\delta v_{SV}/v_{SV}^0$, $\delta v_{PH}/v_{PH}^0$, and $\delta v_{PV}/v_{PV}^0$ can be retrieved from $\delta v_S/v_S^0$, $\delta a_S/a_S^0$, $\delta v_P/v_P^0$, and $\delta a_P/a_P^0$; however, inversions for the two sets of parameters do not yield identical results since the regularization affects different parameters (unless it is modified accordingly). We prefer to invert for the isotropic and anisotropic perturbations because it allows for better control of the smoothness of anisotropic variations, which are thought to reflect large-scale dynamic processes in the mantle.

[25] As opposed to inversions for older reference models, such as PREM, we implement a new technique, which allows for a much better data fit. Instead of inverting

directly for a spherically symmetric model, we first invert for a 3-D model and then calculate the new 1-D reference model as a spherical average of the 3-D model. In this study, we invert for 3-D variations only in shear wave velocity and anisotropy. Perhaps improved data in the future will also allow for inversions for 3-D variations in compressional wave velocities, η, and density. At this point, however, we believe that we cannot resolve lateral variations in these parameters robustly. Inverting independently for radial variations in all parameters, on the other hand, is necessary to fit the data. In summary, we solve independently for 3-D variations in shear wave velocity and anisotropy, 1-D variations in compressional wave velocity and anisotropy, η, and density, as well as centroid moment tensors (CMTs) [*Dziewonski et al.*, 1981; *Dziewonski and Woodhouse*, 1983] for all earthquakes. Lateral variations in shear wave velocity and anisotropy are expanded over 362 spherical splines [*Wang and Dahlen*, 1995] and the vertical variations are parameterized by 16 radial cubic B-splines (Figure 3). Since we do not include normal-mode data in the inversion,

the model is heavily damped in the lower mantle so that the 1-D shear-wave velocity converges to PREM at a depth of 1320 km. The sensitivity to the compressional wave velocities, η, and density comes primarily from the waveforms. The choice of the number of B-splines used to parameterize the compressional-wave velocities and the density is a compromise between the limited sensitivity of our data and the necessity to correct the starting model in the transition zone and lower mantle. The density and v_P converge to PREM as the amplitude of the lower mantle spline converges to zero at 1320 km. We find η and anisotropic variations below 220 km to be small and constrain them to vanish at 410 km by using only the four uppermost splines. Density perturbations $\frac{\delta \rho}{\rho_0}$ are additionally constrained to match the total mass $M = 5.974 \ 10^{24}$ kg and moment of inertia $I = 0.3308 \ M \ (6371 \ \text{km})^2$ of the Earth, as in PREM. The data are allowed to control the jumps in all parameters at the 650-km discontinuity because the radial parameterization is split at this depth. The radial splines are continuous elsewhere hence the jumps at other discontinuities are fixed to the values defined in the starting model.

[26] Because our model is represented in terms of the finite number of basis functions, we apply discrete inverse theory [*Menke*, 1989] to solve the inverse problem. We calculate a weighted least-squares solution using a standard Cholesky factorization for positive definite matrices [*Trefethen and Bau*, 1997] and minimize vertical and horizontal gradients, as well as the norm of the solution to stabilize the inversion.

[27] The new reference model is obtained through iterative inversion of all our data except for the measurements of the SS precursors. In the first iteration, we solve for perturbations with respect to the starting model. The solution is then used as a reference model in the second iteration and the convergence can be achieved after three iterations. Fitting the waveform data requires the 1-D model to be developed as a spherical average of a 3-D model at each iteration. Each iteration involves several subiterations of waveform inversion, as in the determination of a 3-D model discussed in section 4. Consequently, the computational cost required to develop the new reference model is high, which precludes performing rigorous tests of resolution or uniqueness. Instead, we have performed a series of inversions and identified features of the model that appear to be preferred by the data and those that more strongly depend on the regularization. In the following section, we discuss both types of features.

3.2. New Reference Model

[28] The following features of the new reference model STW105 are only weakly dependent on regularization and therefore are considered to be robust. Shear wave velocities are the best constrained parameters in the inversion. The new model, unlike PREM, shows the maximum shear wave anisotropy at 120 km depth, which decreases at shallower depths (Figure 4). In order to fit the waveform data as well as PREM, η must be less than one in the top ~200 km of the mantle. As an example, the P-SV body wave waveforms calculated assuming that $\eta = 1$ have a root-mean-square (rms) misfit higher by 0.1 than the seismograms obtained with the appropriate η. For Rayleigh waveforms, our preferred model lowers the average misfit by 0.04 compared

to the model with $\eta = 1$. Compressional-wave velocities in the uppermost 300 km of the mantle must be ~2-5% lower than in the starting model in order to fit the data as well as PREM. Even when we allowed for anisotropy at all depths in the upper mantle, we found, in agreement with PREM, that significant anisotropy is not required by the data below ~220 km. We constrained anisotropy in STW105 to vanish at 410 km.

[29] The following features of STW105 depend more strongly on the regularization. We find that the strength of anisotropy of compressional waves trades off with the density, which has been also suggested by *Beghein et al.* [2006]. It also trades off with η, and it is not clear whether it is indeed different than the shear wave anisotropy. The average P_n velocity in STW105 is lower than in PREM and more similar to that in the model ak135 [*Kennett et al.*, 1995], which was constrained by P and P_n data. The sign of the dv_P/dr gradients in the uppermost 200 km of the mantle is not well resolved by surface wave data. The details of the density profile also depend on regularization, and we find that the positive $d\rho/dr$ gradient found at shallow depths in PREM is not required to fit the data. The elevation of the discontinuity between the upper and lower mantle from 670 km to 650 km is compensated for by reduced velocities in the upper mantle and reduced density in the lower mantle. The radial resolution in this depth range is, however, poor, and the velocity and density perturbations tend to be distributed over several hundred kilometers.

[30] We conclude that the 1-D shear wave velocity structure in the upper mantle in STW105 is well constrained by our data. The variations in v_{PH}, v_{PV}, η, and density are less robust, however; inverting for deviations of these parameters from the starting model is necessary for fitting the waveform data at least as well as PREM. STW105 converges to PREM at a depth of 1320 km and in order to improve the model in the lower mantle, it would be necessary to include normal-mode data in the inversion.

4. Global 3-D Shear Wave Velocity Model
4.1. Parameterization and Inversion

[31] Our new 3-D model is, with a few exceptions discussed in what follows, calculated using the same data and methods as the reference model STW105. The data set in the 3-D inversion is extended by adding the measurements of travel times of SS precursors. Since our combined data do not have enough resolving power to resolve lateral variations in five elastic parameters and density independently, we neglect their sensitivity to density and η variations, and further reduce the number of free parameters assuming that $\delta v_{PH}/v_{PH} = 0.55 \ \delta v_{SH}/v_{SH}$ and $\delta v_{PV}/v_{PV} = 0.55 \ \delta v_{SV}/v_{SV}$. We found global averages of v_{SH} and v_{SV} in the new 3-D model to be very similar to those in the 1-D model, which means that it is not necessary to further refine our reference model and recalculate the sensitivity kernels. The scaling of velocity perturbations for both horizontally and vertically polarized waves is equivalent to scaling the isotropic and anisotropic perturbations. The scaling factor of 0.55 for isotropic perturbations is consistent with the anomalies predicted for purely thermal effects [*Karato*, 1993] and with the modeling of compressional and shear wave velocity in the mantle [*Su and Dziewoński*, 1993;
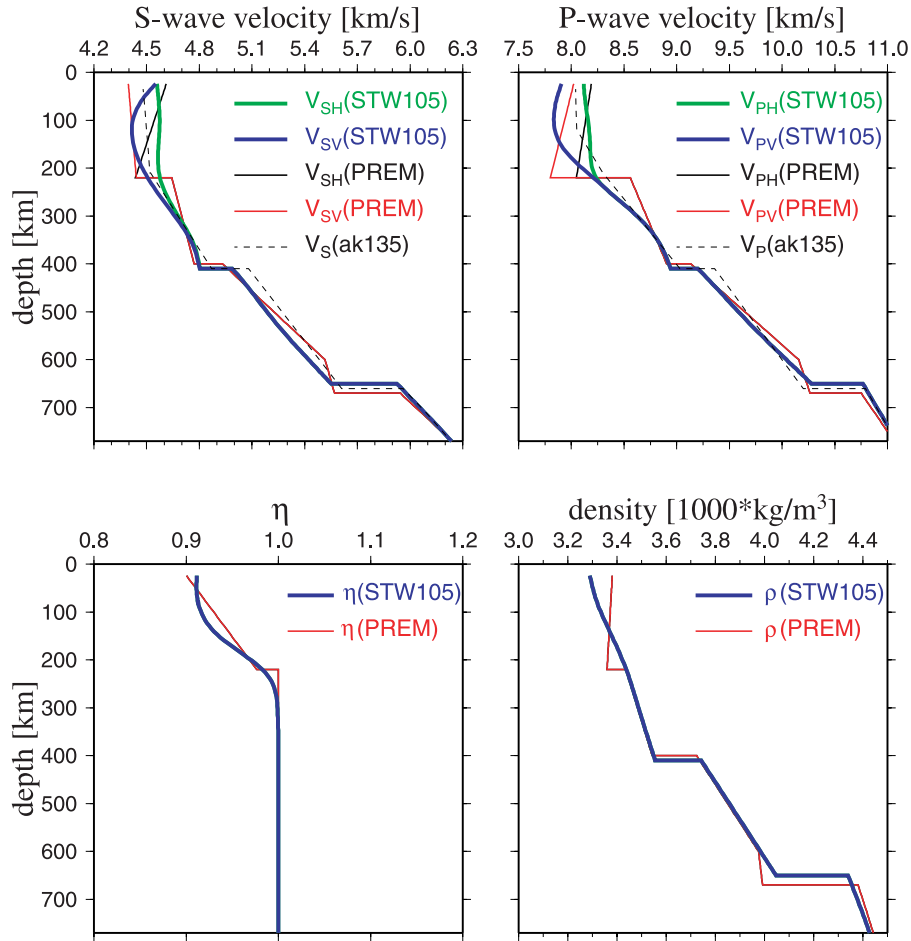
Figure 4. The new reference model STW105 plotted with PREM [*Dziewoński and Anderson*, 1981] and ak135 [*Kennett et al.*, 1995]. Our new reference model STW105 is continuous at 220 km. Shear wave anisotropy is maximum at about 120 km and becomes very weak below 220 km. The profile of η is consistent with PREM. The average v_P at shallow depths is slower than in PREM and is more similar to that in the model ak135, which was constrained by P and P_n travel times.

Robertson and Woodhouse, 1996]. The more recent tomographic studies [*Su and Dziewoński*, 1997; *Masters et al.*, 2000], however, indicate that the scaling factor may be about two times lower in the lowermost mantle. Our data do not have enough resolving power to determine the scaling factor; however, we obtain nearly identical models for assumed values of 0, 0.55, and 1. Petrological [*Montagner and Anderson*, 1989] and geodynamic [*Becker et al.*, 2008] constraints suggest that the compressional and shear wave anisotropy are also correlated.

[32] As in the derivation of the reference model, we invert for isotropic (equation (4)) and anisotropic (equation (5)) variations in shear wave velocity rather than for $\delta v_{SH}/v_{SH}$ and $\delta v_{SV}/v_{SV}$. This approach allows us to control the roughness of both isotropic and anisotropic velocity variations.

[33] Variations in shear wave velocity and anisotropy, as well as topographies of the transition zone discontinuities, are parameterized horizontally in terms of 362 spherical splines. To describe isotropic velocity variations in the radial direction, we use 16 B-splines split at 650 km, as in Figure 3. In our preferred model S362ANI, we constrain anisotropy to vanish at 410 km by solving for coefficients corresponding to the uppermost four splines. In section 4.3, we also attempt to constrain the anisotropic variations in the whole mantle using all 16 splines.

[34] Figure 5 shows how different data sets constrain the model in different depth ranges in the mantle. The sensitivity corresponding to each radial spline is defined, as in the work of *Gu et al.* [2001a], as a global average of the diagonal elements of the inner product matrix $A^T A$. Compared to *Gu et al.* [2001a], our plot does not involve any normalization and is extended by adding anisotropy and topography sensitivities, as well as the cumulative sensitivities for three main subsets of data and for all data combined. The structure of the uppermost mantle is determined primarily by short- and intermediate-period surface waves. In the transition zone, the model depends primarily on the waveforms, which show much higher sensitivity for vertical and longitudinal components than for the transverse component. Consequently, determination of the anisotropic structure at the bottom of the upper mantle may be difficult. Velocities in the lower mantle are determined primarily by the diverse set of travel times of teleseismic body waves. The D″ region is best sampled by horizontally polarized S waves diffracted at the core–mantle boundary, which are sensitive only to variations in v_{SH}. The SKKS−SKS and
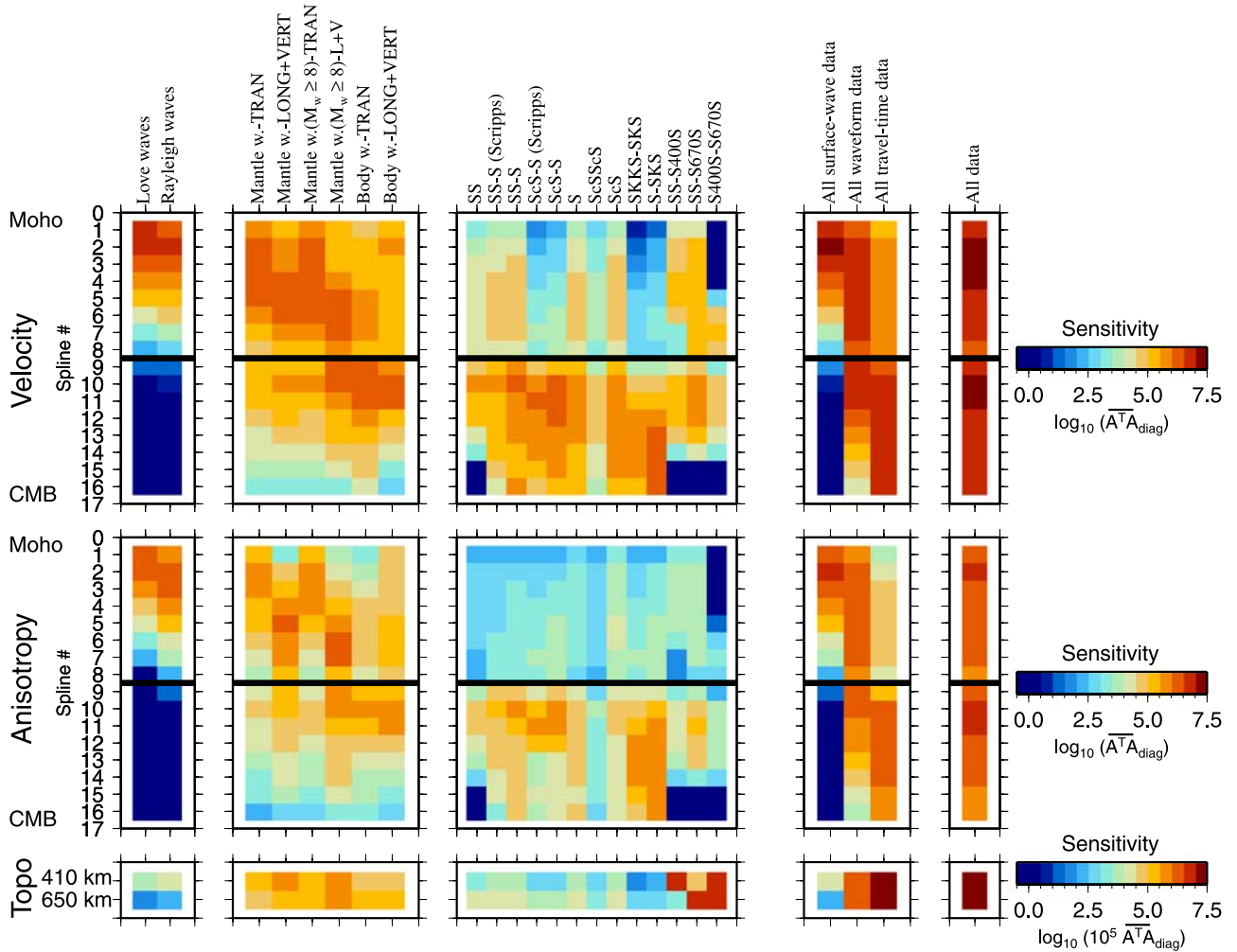
Figure 5. Sensitivity of different data sets calculated as global averages of the diagonal elements of the inner-product matrix $A^T A$ for every cubic spline and for topographies of the transition zone discontinuities. The inner product matrices are weighted in the same way as in the inversion for the global three-dimensional model. The panels on the right show cumulative sensitivities for surface wave, waveform, and travel time data, and for all data combined. LONG, TRAN, and VERT indicate longitudinal, transverse, and vertical components of a seismogram, and "w." denotes waveforms. A different scale was used for the topography sensitivity since it is much smaller than the velocity and anisotropy sensitivities.

S−SKS times are sensitive to both v_{SH} and v_{SV}, and to constrain anisotropic variations at the bottom of the mantle, we give these data large weights in the inversion. Topography of the transition zone discontinuities is determined primarily by travel times of SS precursors. Long-period waveforms are also significantly sensitive to perturbations in discontinuity depths. Despite low lateral resolution, this sensitivity allows for correcting the velocities and density in the new reference model for the effect of shifting the discontinuities with respect to PREM.

[35] Diagonal elements of each $A^T A$ matrix shown in Figure 5 are multiplied by the same weighting factors as those used in the inversion. We select weights that allow us to constrain all splines as uniformly as possible. The maximum velocity sensitivity, which is observed for radial splines 2 and 10, is only 10 times higher than for the most weakly constrained spline 8 at the bottom of the upper mantle.

[36] Sensitivity kernels for all data are calculated using STW105. Since inversions of surface wave phase anomalies and teleseismic body wave travel times are only weakly nonlinear, we calculate the inner product matrices and data vectors for these data sets only once. In contrast, the waveform inversion is strongly nonlinear and has to be solved iteratively. The data vectors for waveforms and CMT solutions are updated as we improve the 3-D model. In the first iteration of waveform inversion, we calculate synthetic seismograms using the Harvard CMT solutions [e.g., *Ekström et al.*, 2005]. We then accumulate the data and regularization inner product matrices and data vectors and invert them jointly for the velocity structure and discontinuity topographies. The new model is then used to determine new CMT solutions, the structural kernels are updated and accumulated, and convergence is achieved after several iterations.

[37] Since models regularized by norm damping have a tendency to correlate with the noneven data coverage typical
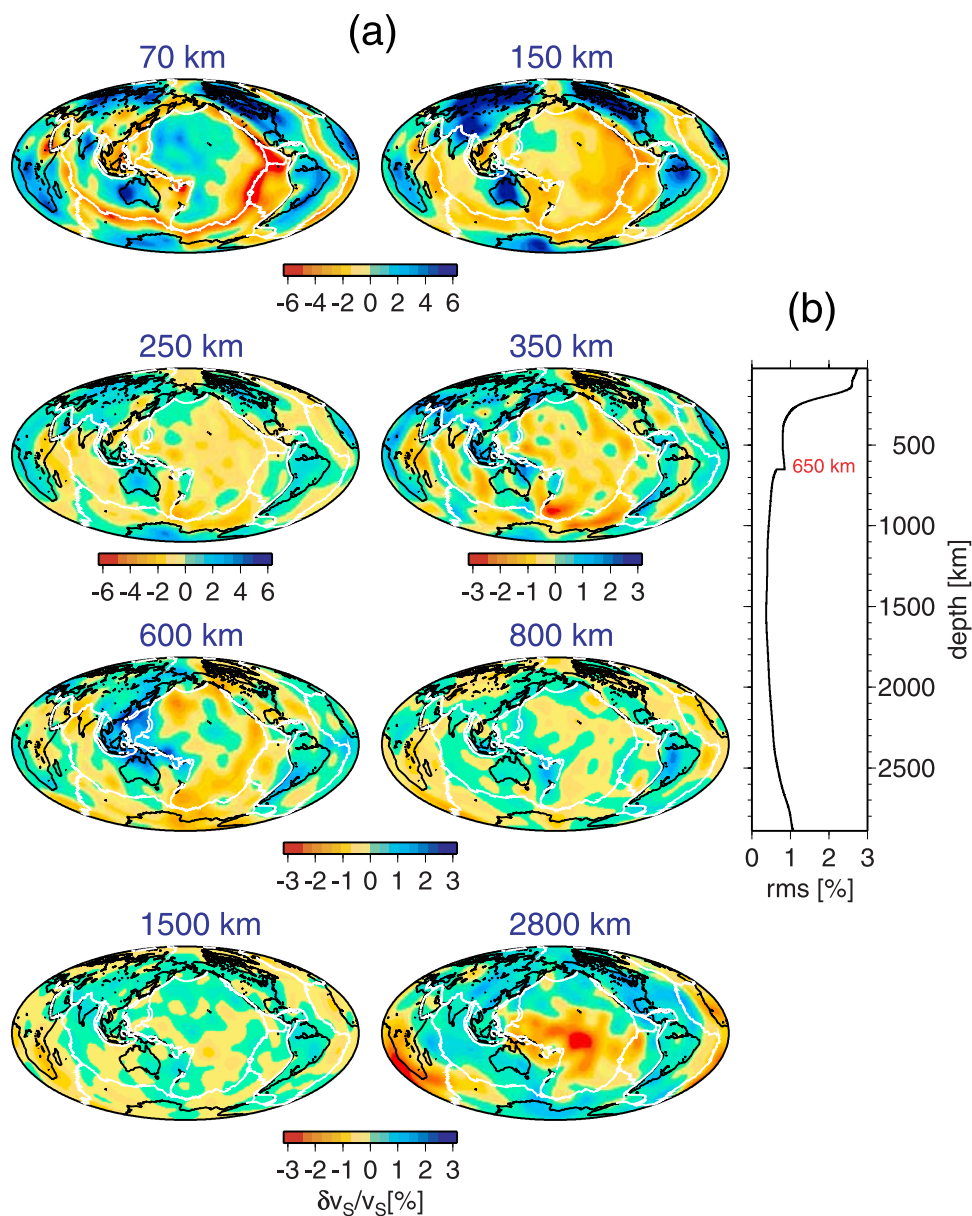
Figure 6. (a) Isotropic velocity anomalies $\delta v_S^{Voigt}/v_S^{Voigt}$ in our new model S362ANI. Perturbations in S362ANI are defined with respect to STW105 and plotted with the global average removed. The white lines show plate boundaries. (b) Amplitude of root-mean-square isotropic velocity variations in S362ANI.

for global mantle tomography [*Boschi and Dziewoński*, 1999], we choose to minimize only vertical and horizontal roughness but not the norm of the solution. We invert for perturbations with respect to the 1-D model STW105 rather than for perturbations with respect to an existing 3-D model. We prefer this approach since it yields a solution that is smooth with respect to a 1-D model STW105, whereas the latter approach would minimize smoothness or norm with respect to an arbitrarily chosen, imperfect target model.

4.2. Isotropic Variations

[38] The overall isotropic shear wave velocity structure in the mantle, as constrained by our preferred model S362ANI, is shown in Figure 6a. At a depth of 70 km, the

pattern of heterogeneity is dominated by negative anomalies as strong as −7%, which are very closely aligned with the mid-ocean ridges and regions of back-arc extension. The mid-ocean ridge signatures extend down to at least 150-km depth and vanish at 200−250 km. Away from the plate boundaries, the oceanic anomalies can be positive at 70 km and may become negative at 150 km, as in central Pacific. The strongest velocity anomalies at 150 km are observed beneath continents. At 250 km, differences between continents and oceans are much weaker, and the depth range between 250 and 400 km depths is significantly less heterogeneous than the uppermost mantle. One of the most pronounced features at 350 km depth is a slow velocity anomaly south of New Zealand. It is located away from the

known hot spots, as pointed out by *Ritsema and Allen* [2003], as well as from the mid-ocean ridges, and its origin is not clear. In the transition zone, up to +3% anomalies are observed beneath major subduction zones but below the 650-km discontinuity they are less than half as strong, with the exception of anomalies beneath South America and the South Fiji Basin. As a consequence, the upper mantle–lower mantle boundary is characterized by a sudden drop in the rms lateral variations (Figure 6b). The faster-than-average velocities beneath subduction zones nearly vanish in the middle mantle. In the lowermost mantle, S362ANI is dominated by large-scale slow-velocity anomalies beneath the Pacific and Africa, usually referred to as superplumes, which have been known since the first P-velocity tomographic studies [*Dziewoński et al.*, 1977; *Dziewoński*, 1984]. These superplumes are up to 3.5% slower than average, while the surrounding positive anomalies reach only +1.9%.

[39] Resolution tests for the isotropic and anisotropic shear wave velocities performed by, for example, *Panning and Romanowicz* [2006] and for topographies of the transition zone discontinuities [*Gu et al.*, 2003] suggest that large-scale structures in the mantle may be recovered by data used by these authors. Our data set is significantly larger than that of *Gu et al.* [2003] and comparable with that of *Panning and Romanowicz* [2006], and the wavelength of anomalies in S362ANI is comparable with the other two models. Only long-wavelength features are discussed in this paper and therefore instead of repeating the resolution tests, we find it more instructive to compare S362ANI with two models obtained from diverse data sets by different researchers from different types of measurements using different modeling techniques. The comparison should help to identify persistent features that are independent of arbitrary choices of the regularization, data weights, and modeling technique. The first of the two models, S20RTS, was obtained by *Ritsema et al.* [1999] from the measurements of fundamental-mode and overtone surface wave velocities analyzed with distinct sensitivity kernels along the paths, body wave travel times, and normal-mode splitting data. The second model, SAW642AN, is that of *Panning and Romanowicz* [2006], who inverted surface and body wave waveforms using NACT.

[40] Figure 7 demonstrates that the three models are very well correlated down to 250-km depth even for anomalies as small as 1000 km. The total correlation between S362ANI and S20RTS is higher than 0.5 in the whole mantle and even higher for spherical harmonic degree two. Lower total correlations between SAW642AN and the other two models is observed at 400 km and in the middle mantle, but at degree-two, SAW642AN agrees well with S20RTS in the whole mantle, and with S362ANI everywhere except the middle mantle. In all models the root-mean-square variations are stronger above the 650-km boundary than below this boundary. In particular, the power of the degree-two anomalies shows a significant maximum in the transition zone. Differences in the amplitude in different models result from choosing continuous versus split radial parameterization.

[41] At a depth of 150 km, our model S362ANI, and models SAW642AN and S20RTS show up to +8% anomalies beneath continents, while at 250 km, all models are up to 3% faster than average in continental regions (Figure 8). The abrupt decrease in the strength of the anomalies may

mark the base of the continental lithosphere. The velocities in the suboceanic asthenosphere are appreciably lower than beneath the continents even at 250 km. All three models show +2–3% anomalies beneath major subduction zones in the transition zone, whose amplitudes diminish below the 650-km discontinuity. The abrupt changes in the strength and dominating wavelength of heterogeneity at ∼200 and 650 km depths are clearly visible in Figure 9. In the uppermost 200 km of the mantle, the spectra are dominated by the lowest 5–6 degrees representing strong anomalies of continental-size, or larger. Below 250 km, the power spectra are weaker and white, the degree-two amplitudes increase in the transition zone, and nearly vanish in the uppermost lower mantle. The transition zone therefore appears to be the third significantly heterogeneous layer in the mantle, in addition to the two boundary layers at the top and bottom of the mantle. It is difficult to attribute such characteristics to imperfect or subjective modeling approach, since it is observed in three different models. In particular, the dramatic change in the power spectrum between 600 and 800 km is observed not only in S362ANI, in which the radial parameterization is split at 650 km, but also in S20RTS and SAW642AN, in which the radial parameterizations constrain the models to be continuous at this boundary. In S20RTS and SAW642AN, the change in power spectra is therefore likely to be underestimated. The lower mantle spectra are, in general, dominated by the degree-two superplumes but certain differences between the models are observed. SAW642AN is devoid of power at degrees higher than five in the middle mantle, a feature likely to be caused by damping. The spectra in S362ANI and S20RTS, on the other hand, are essentially white for degrees higher than three. In S362ANI and SAW642AN, not only degree-two but also degree-three anomalies are slightly stronger than anomalies of different wavelengths. The power at degree one in SAW642AN changes more rapidly with depth than in the other models. Below 2800 km, SAW642AN shows increase in power at all degrees except degree two, and these variations are not well correlated with the other two models (Figure 7). SAW642AN also shows low correlation with other models at 400-km depth, where it is characterized by a strong degree-five component.

4.3. Where Is the Mantle Anisotropic?

[42] As in the case of isotropic structure, we prefer to test the robustness of the anisotropic variations by comparing different tomographic models rather than repeating a resolution test performed by, for example, *Panning and Romanowicz* [2006]. In this section, we compare our model only with SAW642AN, since S20RTS, discussed in section 4.2, is isotropic. Furthermore, instead of presenting our preferred model S362ANI, in which anisotropy is confined to the four uppermost splines, we discuss a whole-mantle anisotropic version S362WMANI. Isotropic and anisotropic variations in S362ANI are nearly identical to those in S362WMANI at all depths where they are allowed.

[43] At 80 and 150 km, S362WMANI shows a strong anisotropy anomaly in the Pacific (Figure 10a), first described by *Ekström and Dziewoński* [1998]. The $v_{SH} > v_{SV}$ pattern at 150 km is also observed beneath the Pacific in SAW642AN, but the sign of this anomaly does not change at 80 km, in contrast to S362WMANI. This may be a conse-
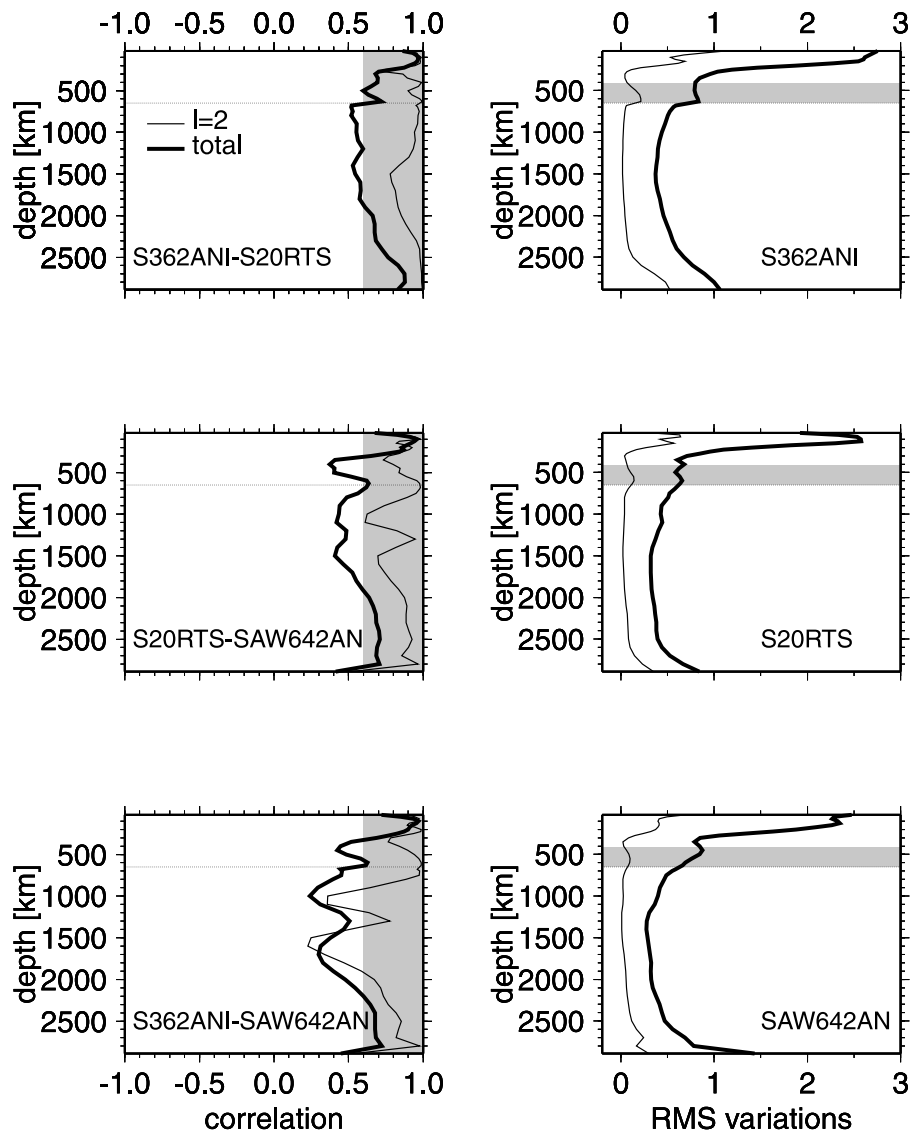
Figure 7. (left) Correlations and (right) power of isotropic velocity variations in models S362ANI, S20RTS, and SAW642ANI. Thick lines indicate the total correlations and root-mean-square variations, while thin lines indicate the correlations and power for spherical-harmonic degree two. The shaded areas indicate correlations higher than 0.6 in the left column and the mantle transition zone in the right column.

quence of not including surface waves of periods shorter than 60 s in SAW642AN, which may lead to limited radial resolution above 100 km. At 300 km, we find, in agreement with *Panning and Romanowicz* [2006], a $v_{SH} < v_{SV}$ anomaly beneath the East Pacific Rise. The predominantly $v_{SH} > v_{SV}$ anisotropy beneath continents reported by *Gung et al.* [2003] is observed in SAW642AN, but it is less pronounced in our model. At 500 km, *Panning and Romanowicz* [2006] find slightly faster v_{SV} than v_{SH} beneath mid-ocean ridges, a pattern inconsistent with S362WMANI. In the middle mantle, the anisotropy is much weaker and the two models are poorly correlated (Figure 10b). Anisotropy becomes stronger in the D″ region and both models show negative anomalies at the slow-velocity superplumes. The correlation between the isotropic and anisotropic anomalies in the lower mantle is especially high in SAW642AN (Figure 10c). On the other hand, the correlation is close to zero at almost

all depths in S362WMANI. We conclude that anisotropic variations in the two models are consistent only at 150-km and 2800-km depths.

[44] To further test the robustness of our whole-mantle anisotropic model, we perform two experiments. First, we investigate whether anisotropy is required by the data at different depths in the mantle. Figure 11 summarizes the data fits for three different models: S362WMANI with anisotropy allowed at all depths in the mantle, S362ANI with anisotropy confined to the uppermost mantle, and S362ISO with no lateral anisotropic variations. Including anisotropy clearly improves the fit to the surface wave data, which control the model down to ∼300 km. Anisotropy in the uppermost mantle does not significantly affect the variance reduction for waveforms and body wave travel times since these data have their maximum sensitivity at larger depths. The fit for the waveforms, which control the
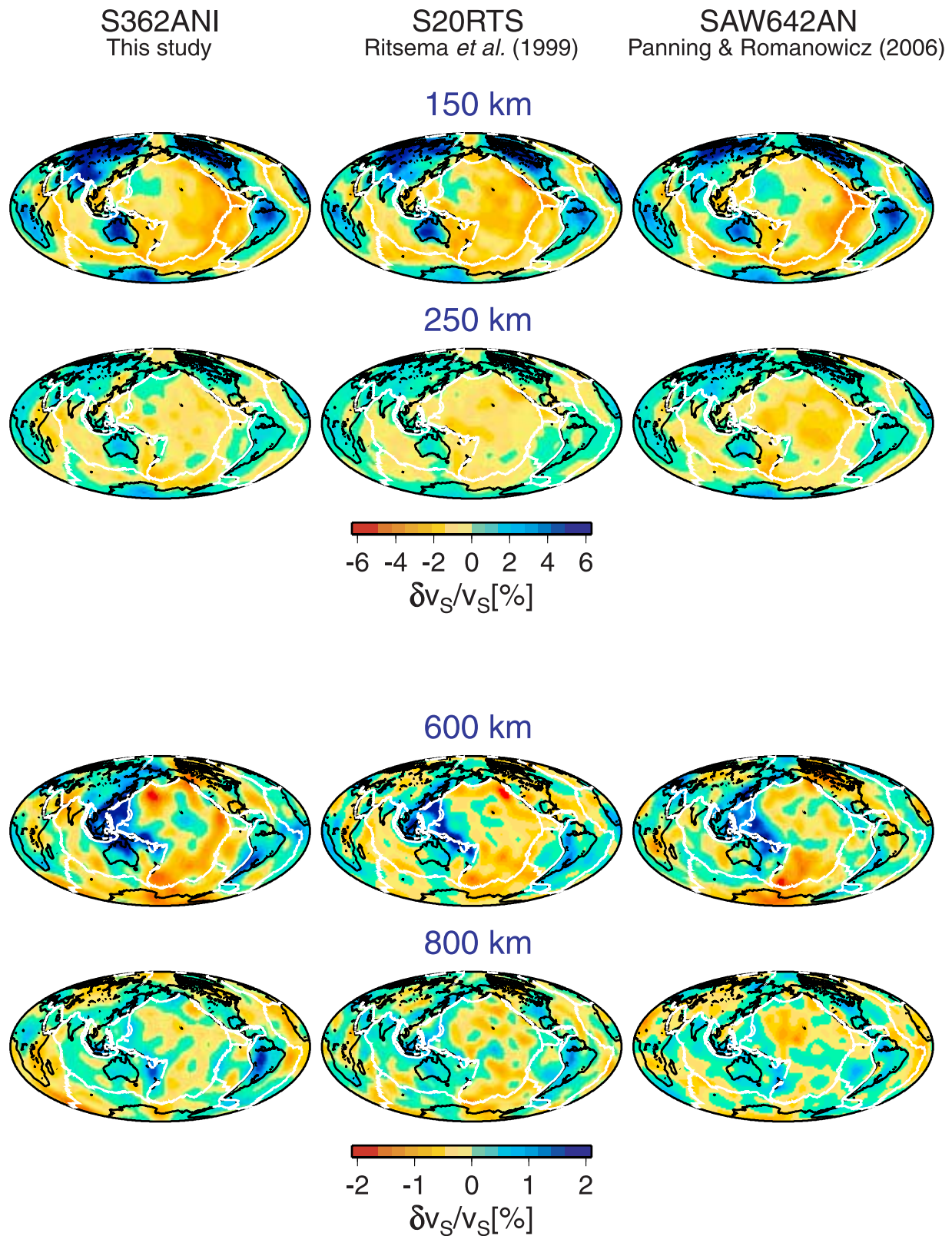
Figure 8. Isotropic shear wave velocity perturbations at 150, 250, 600, and 800 km depths in S362ANI, S20RTS [*Ritsema et al.*, 1999], and SAW642AN [*Panning and Romanowicz*, 2006]. For both anisotropic models S362ANI and SAW642AN we plotted $\delta v_S^{Voigt}/v_S^{Voigt}$. The decrease in positive anomalies between 150 and 250 km depths may represent the base of the continental lithosphere. Strong fast-velocity anomalies are observed beneath major subduction zones in the transition zone but not in the uppermost lower mantle, which suggests that slabs may deflect horizontally or accumulate in the transition zone.
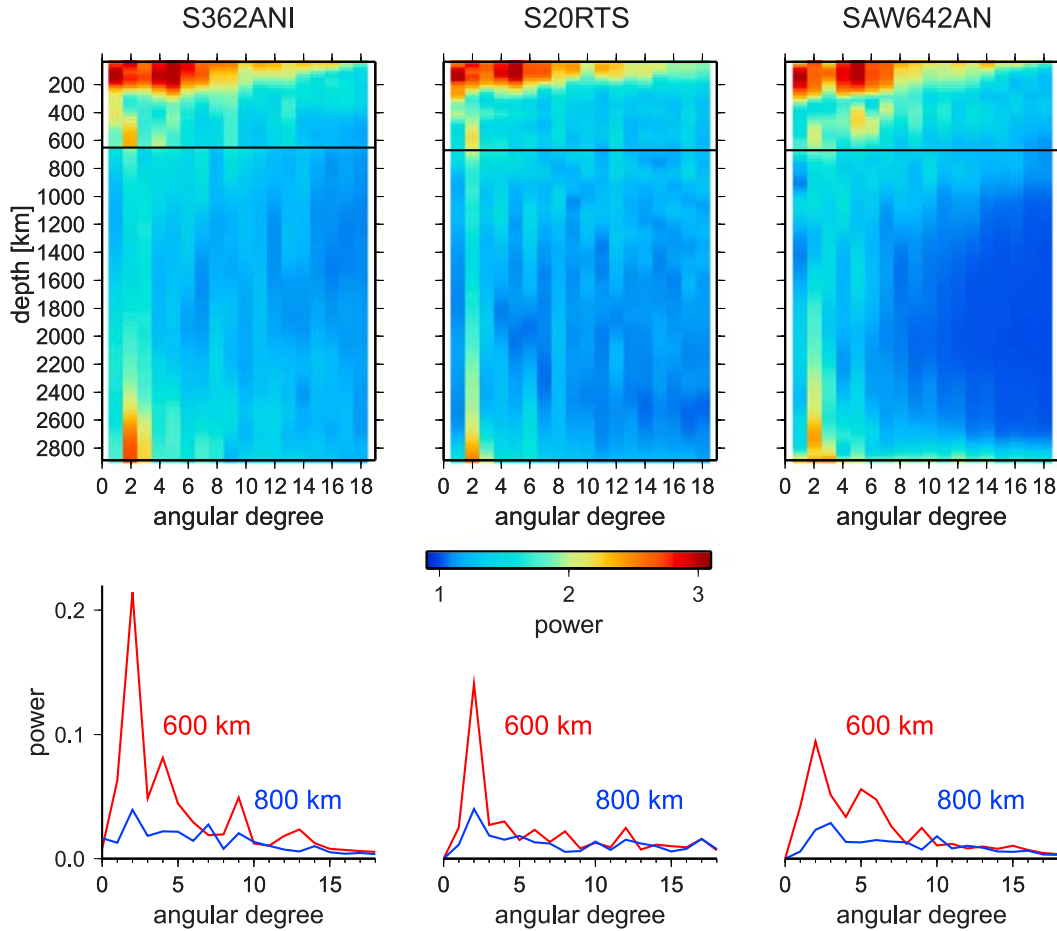
Figure 9. Power spectrum of shear wave velocity heterogeneity in S362ANI, S20RTS [*Ritsema et al.*, 1999], and SAW642AN [*Panning and Romanowicz*, 2006] plotted using a logarithmic color scale. The black line in the upper panels indicates the upper mantle–lower mantle boundary. All three models, which are well constrained in the transition zone by different type measurements of overtones, show a significant change in the power spectrum at this boundary. In particular, a strong maximum at degree two is observed at the base of the transition zone but not in the lower mantle. The change in the power spectrum between the upper and lower mantle is more pronounced when a linear scale is used, as shown in the bottom panels.

model in the transition zone is, however, not appreciably improved even when anisotropy is allowed in the whole mantle. Whole-mantle anisotropy reduces the variance for some travel time data, especially those sampling the lowermost mantle. In particular, the SKKS–SKS residuals show a dramatic improvement. We find that this improvement is only partially caused by the reduction of the average shift between the SKKS and SKS residuals attributed to the core signal by *Liu* [1997], and it remained large even when we removed the average from the SKKS–SKS residuals.

[45] Second, we investigate whether lateral anisotropic variations, such as those in S362WMANI, could be obtained through a velocity–anisotropy tradeoff. To address this problem, we create synthetic data predicted by the isotropic part of S362WMANI. Since the perturbations are likely to be underestimated owing to the regularization applied in the inversion, we multiply the isotropic coefficients $\mathbf{m}_{S362WMANI}^{ISO}$ by an arbitrarily chosen and exaggerated factor of three. The synthetic data $\mathbf{d}^{SYN}$ are obtained from $\mathbf{d}^{SYN} = \mathbf{A}\,(3\,\mathbf{m}_{S362WMANI}^{ISO})$, where $\mathbf{A}$ is the data kernel. The synthetic data are inverted for a whole-mantle anisotropic

output model in exactly the same way as we inverted the data for S362WMANI. The anisotropic structure in the output model is an artifact and represents the leakage of the isotropic signal into the anisotropic part of the model. At 2800 km, the similarity between amplitudes and strength of the spurious anisotropic variations (Figure 12d) and those obtained from the data (Figure 12c) is striking and suggests that the latter may be influenced by the tradeoffs. However, the strength of the anisotropic variations in Figure 12d is exaggerated by using a very strong input model. Without multiplying the input model by three, only a fraction of the amplitudes would be recovered. At 150 km, the range of spurious anisotropic variations is smaller than 2% (Figure 12b), while the range of the variations in S362WMANI exceeds 6% (Figure 12a). The two patterns are not similar to each other, which clearly indicates that the anisotropy in neither S362WMANI nor S362ANI is caused by tradeoffs.

4.4. Effect on the CMT Solutions

[46] To investigate the effect of using our new model S362ANI in the standard CMT source inversions, we
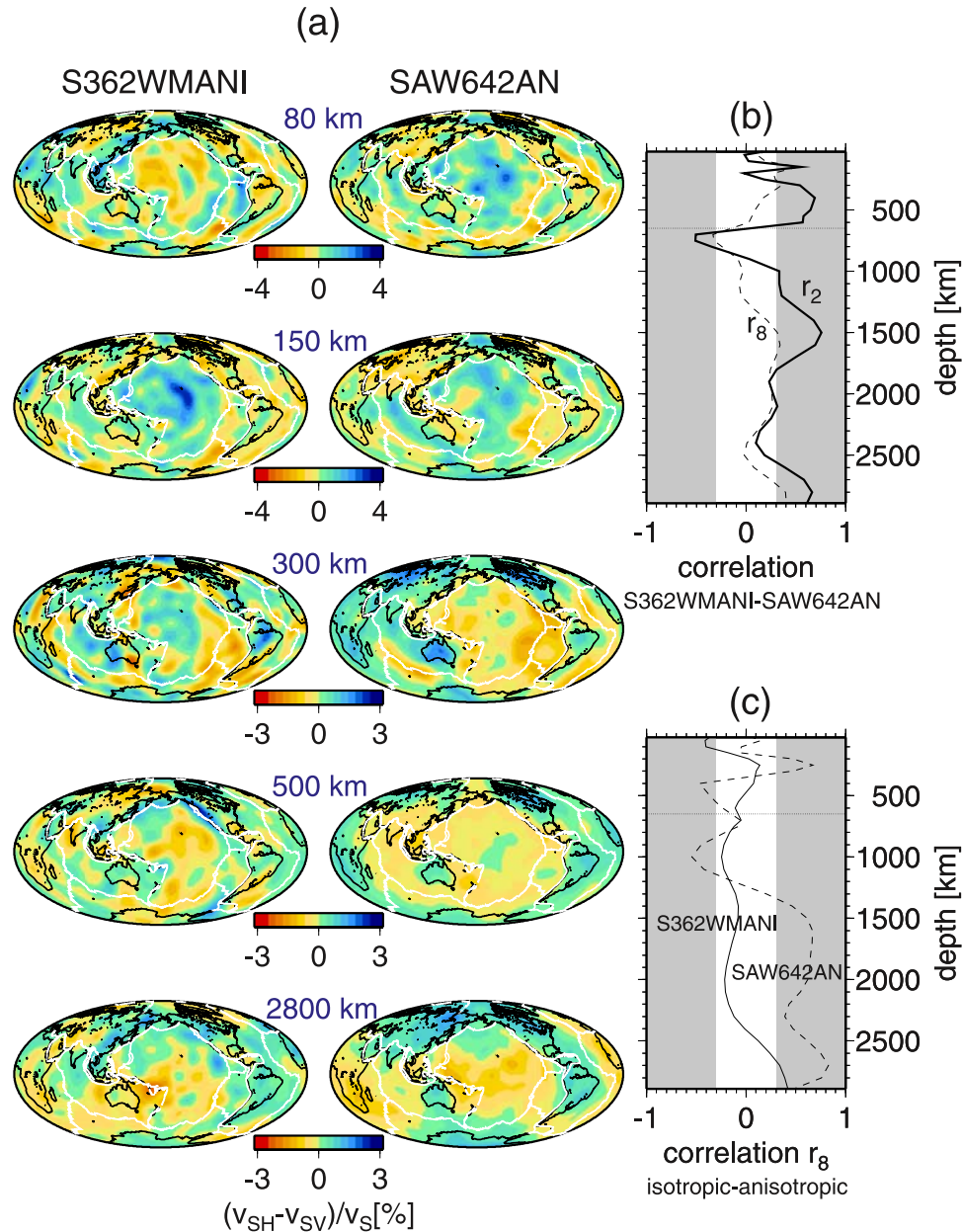
Figure 10. (a) Anisotropic velocity variations $(v_{SH}-v_{SV})/v_S$ in S362WMANI and SAW642AN. Average anisotropy at each depth has been removed in both models to eliminate the effects of different reference models. (b) Correlation between S362WMANI and SAW642AN calculated up to spherical-harmonic degree 2 (solid line) and 8 (dashed line). (c) Correlation between isotropic and anisotropic variations in S362WMANI (solid line) and SAW642AN (dashed line) calculated up to spherical-harmonic degree 8. The dotted lines in Figures 10b and 10c indicate the 650-km discontinuity and the shaded areas indicate correlations lower than −0.3 and higher than 0.3.

performed CMT analyses for 229 earthquakes of $M_w \geq 6.5$, discussed in section 2, using models S362ANI and SH8/U4L8 [*Dziewoński and Woodward*, 1992]. The latter model, which has been routinely implemented in the determination of the standard Harvard CMT solutions, is defined as a perturbation with respect to PREM up to spherical-harmonic degree eight, does not account for lateral anisotropic variations, and was derived from a relatively small data set using linear crustal corrections. The CMT solutions for S362ANI, regardless of higher resolution, anisotropy, a new reference model, and improved crustal corrections,

are, in general, very similar to the SH8/U4L8 solutions. The epicenters are typically shifted by about 10 km (Figure 13). Earthquakes in the Indian Ocean and western Pacific are systematically relocated to the south. The shifts around the Mediterranean basin and Middle East are predominantly in the northwestern direction. The single largest shift of 32 km is observed for the $M_w = 6.4$ event that occurred on 15 June 1995 in Greece. The earthquakes beneath South America tend to move southeast but offshore events are relocated toward the Pacific.
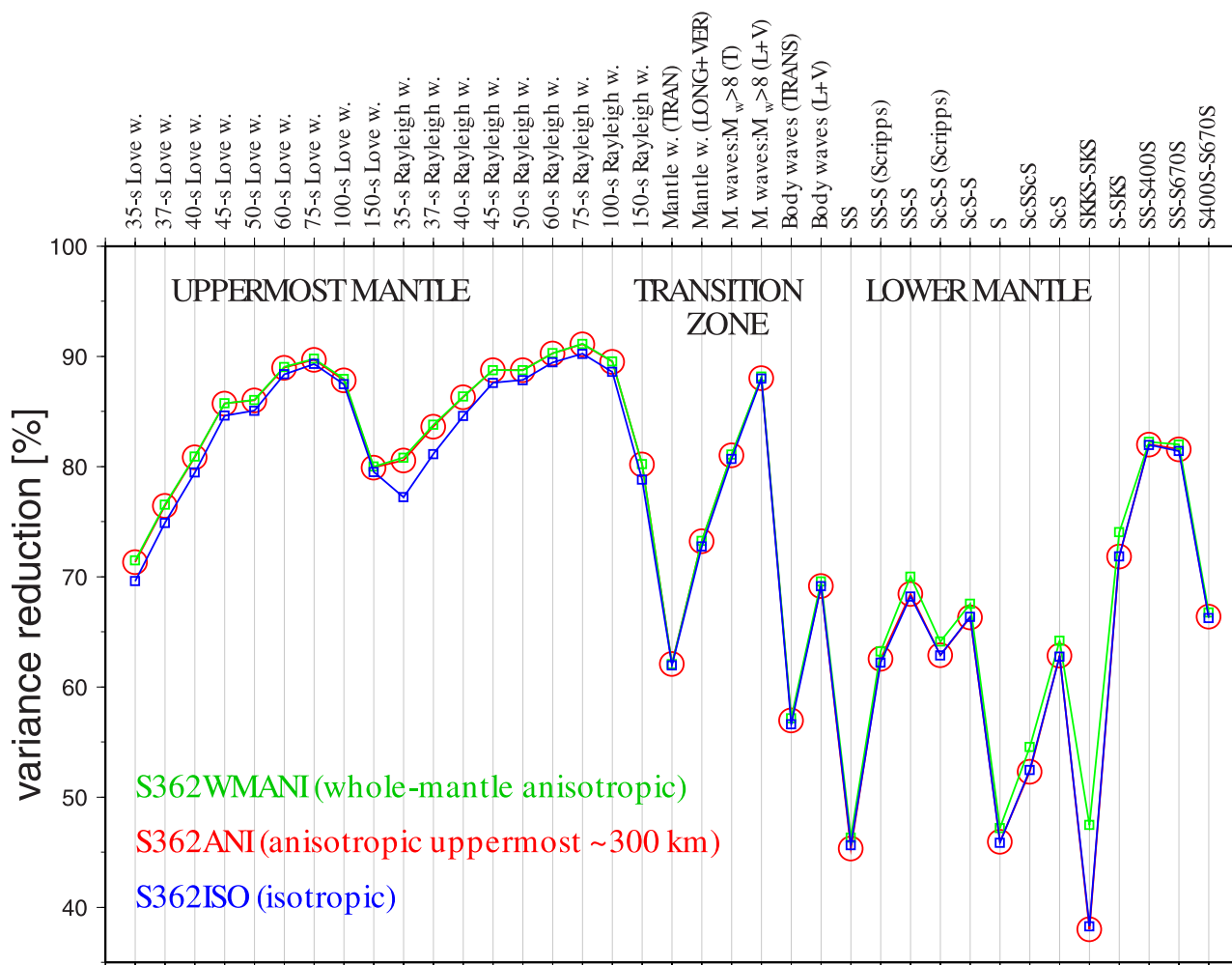
Figure 11. Variance reduction for the whole-mantle anisotropic model S362WMANI (in green), S362ANI with anisotropy confined to the four uppermost splines (in red), and for the model S362ISO without lateral anisotropic variations (in blue). The variance reduction was calculated separately for measurements of surface wave phase velocities at different periods, for different types of waveforms, and different types of body wave travel times. The three data sets constrain anisotropy in the uppermost mantle, transition zone, and lower mantle, respectively. Including anisotropy in the uppermost mantle significantly improves the fit of the surface wave data. The travel time data are fit much better if anisotropy is allowed in the lower mantle.

[47] The depths of events shallower than 300 km are typically increased by a few kilometers for S362ANI, whereas deeper earthquakes are usually pushed slightly shallower. The change in hypocentral depth never exceeds 9 km. Magnitudes for the S362ANI solutions are slightly higher than for SH8/U4L8, but the change in M_w is rarely larger than 0.03 and never exceeds 0.08.

[48] Seismograms calculated for the model S362ANI systematically improve the fit for both mantle and body waves recorded on all components. For many earthquakes, the improvement in rms misfit exceeds 5% and can be as large as 10% for mantle waves and as large as 20% for body waves. However, the median improvement is only 3% for Love waves, 2% for Rayleigh and P-SV body waves, and 1% for SH body waves. The median improvement for different types of waveforms is between 0 and 1% when STW105 is used instead of PREM, between 0 and 0.2% due

to anisotropy in the uppermost mantle, and between 0 and 1% owing to the nonlinear crustal corrections. More detailed discussion of the effect of S362ANI on the CMT solutions can be found in the work of *Kustowski* [2007].

5. Discussion

[49] Persistent long-wavelength patterns observed down to a depth of 900 km in models S362ANI, SAW642AN [*Panning and Romanowicz*, 2006], and S20RTS [*Ritsema et al.*, 1999] appear to be independent of the modeling approach and hence represent robust constraints on the structure of the mantle. In contrast, earlier whole-mantle shear wave velocity models [*Ritsema et al.*, 1999; *Masters et al.*, 2000; *Mégnin and Romanowicz*, 2000; *Gu et al.*, 2001a] exhibit more significant discrepancies, in particular with regard to the depth extent of the continental signatures and heterogeneity in the transition zone. Note that the more
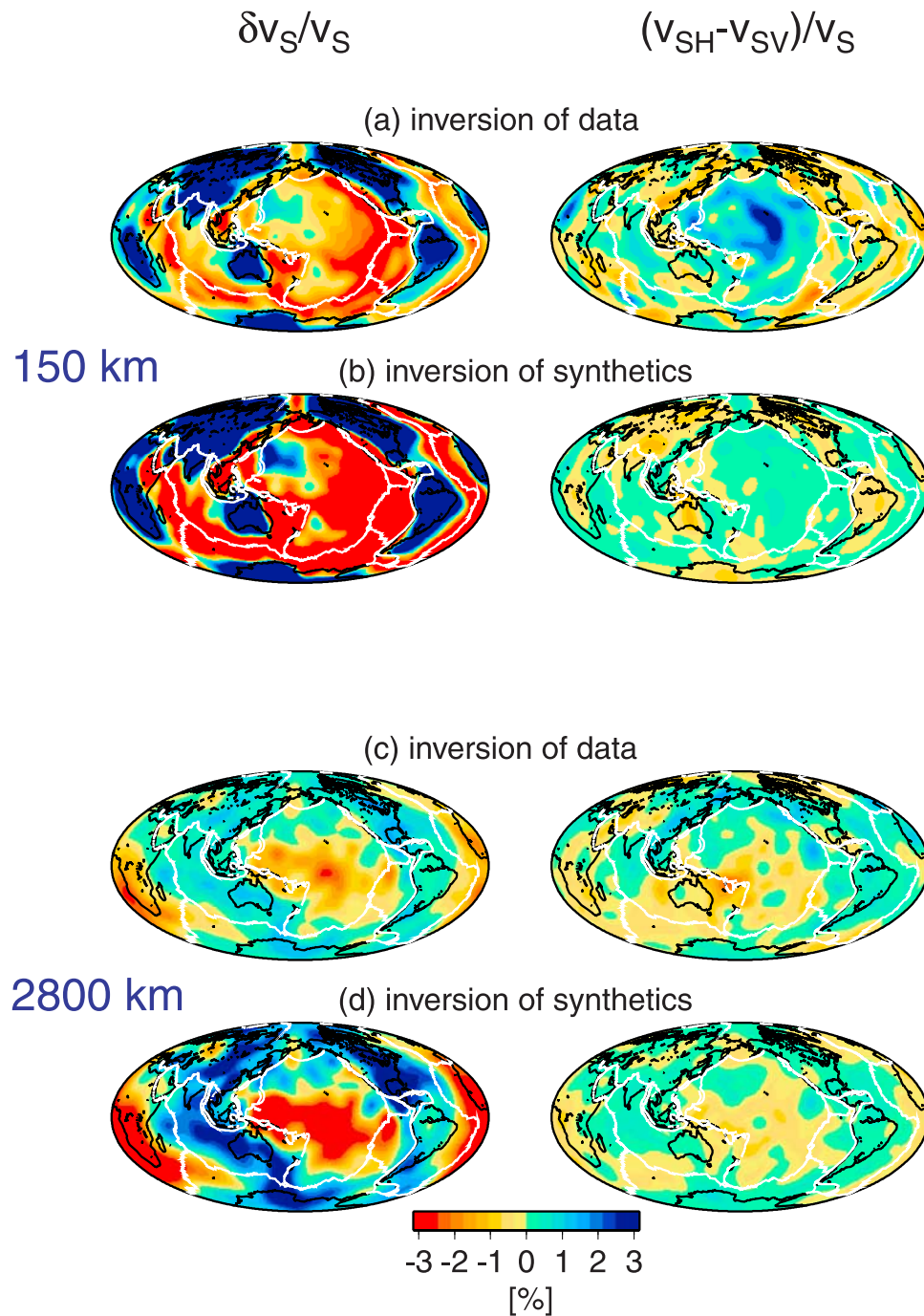
$\delta v_S/v_S$

$(v_{SH}-v_{SV})/v_S$

Figure 12. (a) Isotropic and anisotropic variations in the whole-mantle anisotropic model S362WMANI at a depth of 150 km. (b) Isotropic and anisotropic variations obtained by inverting the synthetic data predicted by the isotropic $3(\delta v_S/v_S)_{S362WMANI}$ input model at a depth of 150 km. (c) and (d) The same as Figures 12a and 12b, respectively, but for a depth of 2800 km. Global averages have been removed. Spurious anisotropic variations are similar to those obtained by inverting the data at a depth of 2800 km but not at 150 km.

recent model of *Ritsema et al.* [2004], although it is not shown in this paper, has not changed dramatically compared to the earlier S20RTS.

[50] The three models S362ANI, SAW642AN, and S20RTS show 3–8% faster than average anomalies beneath stable parts of continents in the uppermost ~200 km of the mantle, underlain by weaker, +1−2% anomalies extending at least to 250 km or even 300 km beneath some cratons. The strong positive anomalies are often interpreted as the cold and stiff continental lithosphere [e.g., *Priestley and Debayle*, 2003], while the deeper anomalies may represent a chemically buoyant or highly viscous continental root. The diminished thickness of the continental lithosphere in S362ANI, SAW642AN, and S20RTS, compared to some
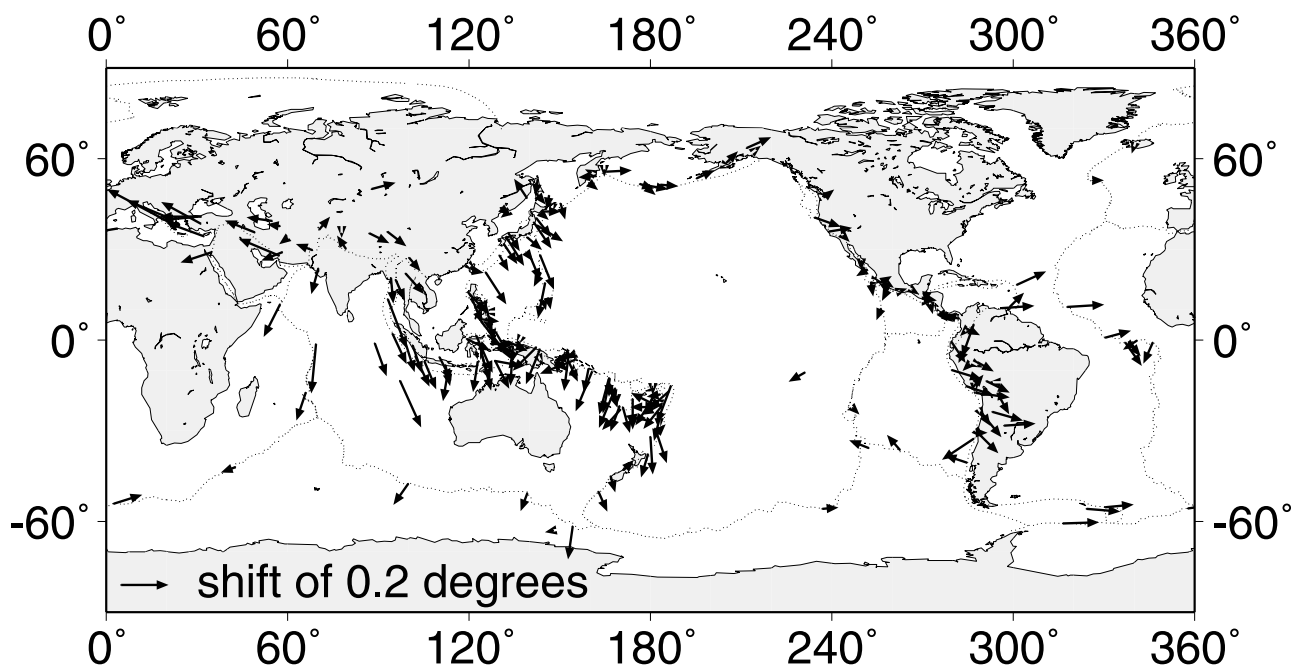
Figure 13. Epicentral shifts for the CMT solutions obtained using S362ANI with respect to the SH8/U4L8 solutions. The length of an arrow is proportional to the shift and the arrow plotted in the lower left corner corresponds to the shift of 0.2 degrees. Dotted lines indicate plate boundaries.

earlier models [*Mégnin and Romanowicz*, 2000; *Gu et al.*, 2001a], may result from the implementation of the nonlinear crustal corrections, as demonstrated by *Kustowski et al.* [2007], and, perhaps, by weaker damping. Thicker continental signatures in the work of *Mégnin and Romanowicz* [2000] might have been caused by using only v_{SH}-sensitive waveforms while the anisotropic effects are separated out in more recent models. Since the base of the high-velocity layer appears at ~200 km depth, our model S362ANI, obtained with STW105 as a reference, should be more useful in constraining the absolute velocities and gradients at the base of the lithosphere than the models calculated on top of PREM. The velocity gradients beneath Eurasia will be further discussed in a subsequent publication [*Kustowski et al.*, 2008].

[51] The most pronounced features of the transition zone in S362ANI, S20RTS, and SAW642AN are ~2–3% faster-than-average anomalies extending horizontally over several hundreds of kilometers beneath major subduction zones, a distance much larger that the width of the subducted oceanic lithosphere. The large lateral extent of these anomalies and the dramatic decrease in their amplitudes below 650-km depth (Figure 14) suggests horizontal flattening of the slabs proposed by *Fukao et al.* [2001] or accumulation of subducted material in the transition zone. Such behavior can be explained by the resistance that slabs encounter at the endothermic phase boundary [*Tackley et al.*, 1993], by slab folding due to high viscosity of the lower mantle [*Gurnis and Hager*, 1988], or accumulation of the chemically buoyant subducted material [*Ringwood and Irifune*, 1988]. We do not rule out that some subducted material, in particular, that beneath South America, Indonesia, and south of Fiji, penetrate into the lower mantle. However, the 650-km discontinuity may not be a minor obstacle that the slabs

encounter before sinking into the lower mantle but a major boundary that perturbs the global flow pattern. This interpretation is supported by the dramatic change in the spectra of S362ANI, S20RTS, and SAW642AN. The strong degree-two anomalies in the transition zone are underlain by a weakly heterogeneous uppermost lower mantle characterized by a white spectrum. This spectral change has been reported previously by *Gu et al.* [2001a], who found long-wavelength anomalies in the entire upper mantle to be much stronger than in the lower mantle. In contrast, the power spectra of S362ANI, S20RTS, and SAW642AN show the transition zone as a distinct layer overlain by a weakly heterogeneous region between 250 and 400 depths (Figure 9).

[52] We find, in agreement with *Shearer and Masters* [1992], *Flanagan and Shearer* [1998], and *Gu et al.* [2003], that major subduction zones are typically correlated with the depressions of the 650-km discontinuity (Figure 14). The depressions, which underlie the slab-like anomalies, are likely caused by the interaction of subduction-related material with the phase boundary characterized by a negative Clapeyron slope (for review, see *Helffrich* [2000]). The depressions extending over thousands of kilometers favor the interaction over a broad area rather than the subvertical penetration of the oceanic lithosphere into the lower mantle. The presence of very deep earthquakes located away from the downgoing slabs, whose principal stress axes deflect horizontally from the slabs [*Lundgren and Giardini*, 1994] also cannot be explained by the uninhibited slab penetration. More arguments supporting decoupling of the flow between the upper and lower mantle have been reviewed by *Hamilton* [2002].

[53] Although isotropic anomalies in our model and that of *Panning and Romanowicz* [2006] are highly correlated, anisotropic anomalies are, with few exceptions, inconsistent

Velocity at 550-km depth

Velocity at 750-km depth

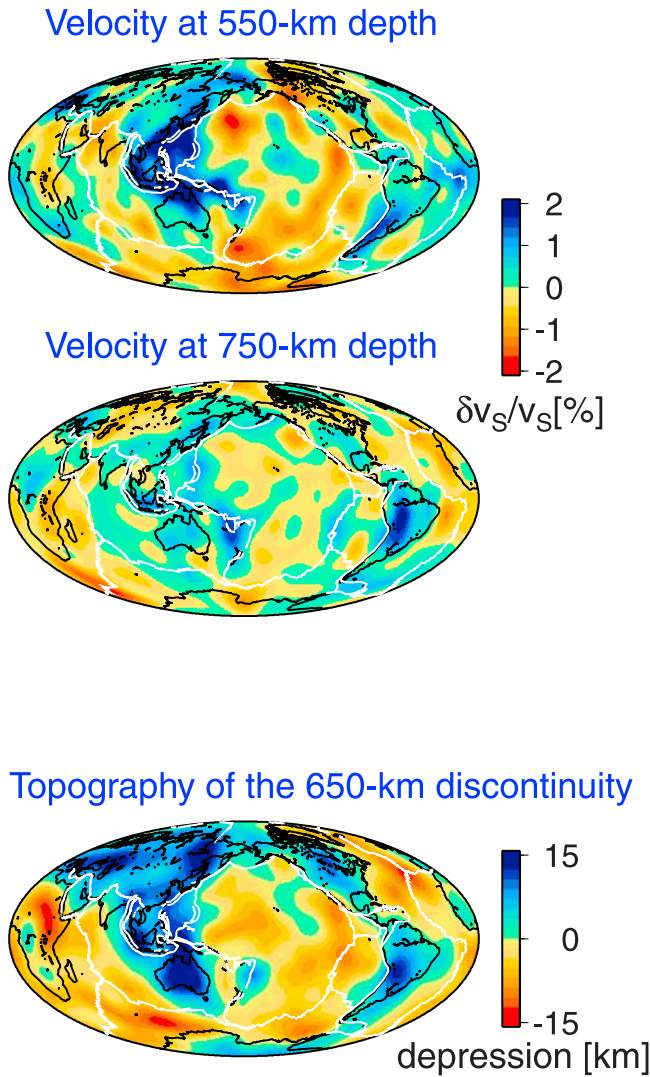## Topography of the 650-km discontinuity

Figure 14. Isotropic shear wave velocity variations above and below the 650-km discontinuity and topography of the 650-km discontinuity in S362ANI.

with each other in the two models. This suggests that the determination of radial anisotropy in the mantle is still an ongoing experiment and only few anisotropic anomalies may be considered robust.

[54] We find the shear wave anisotropy to peak at 120 km and to decrease at shallower depths. This result is different from PREM but similar to the model of *Nettles and Dziewoński* [2008] and roughly consistent with the predictions of the recent flow model of *Becker et al.* [2008]. A strong $v_{SH} > v_{SV}$ anomaly 150 km beneath the Pacific, which was reported by *Ekström and Dziewonski* [1998], is observed not only in our model but also in SAW642AN and in the flow model of *Becker et al.* [2008].

[55] We cannot rule out the presence of anisotropy in the transition zone and the middle mantle but introduction of anisotropy does not appreciably improve the fit to waveforms that are most sensitive to the structure in this depth range. We find the $v_{SH} < v_{SV}$ anomaly beneath the East Pacific Rise described by *Gu et al.* [2005], which may indicate the predominance of the vertical flow. In other regions, we do not reproduce the anisotropic variations in

SAW642AN between 200 and 2600 km depths. Anisotropy improves fits for data sensitive to both the uppermost and the lowermost mantle. The contamination of the isotropic signal into the anisotropic variations is negligible in the uppermost mantle. The superplumes are likely to be anisotropic [e.g., *Kendall*, 2000; *Lay et al.*, 1998]; however, velocity-anisotropy trade-offs may be responsible for one third of the amplitudes of the $v_{SH} < v_{SV}$ anomalies within the superplumes in our inversion. At a 2800 km depth, we find v_{SH} to be, on average, 0.1% faster than v_{SV}, while *Panning and Romanowicz* [2006] reported five times larger difference and attributed it to the predominantly horizontal flow. Estimating the average anisotropy in the D″ region is difficult because of tradeoffs with the compressional-wave velocities in the outermost core, which may be slightly inaccurate in PREM [*Lay and Young*, 1990; *Liu*, 1997].

6. Conclusions

[56] We believe that this work represents progress in estimating the heterogeneity in the mantle for two main reasons. First, we have built our new 1-D and 3-D models from an expanded data set, which reduced the null space and the significance of regularization in the inversion. Second, we have shown that long-wavelength patterns of isotropic shear wave velocity are correlated in recent whole-mantle models, including our model, regardless of using different data and inversion techniques. In contrast, anisotropic anomalies, with few exceptions, show poor correlation. Additional tests are needed to explain whether the discrepancies are due to differences in the measurement techniques, data, matrix conditioning, or velocity–anisotropy tradeoffs.

Appendix A: Body Waves in the Transversely Isotropic Medium

[57] Partial derivatives for the inversion of body wave travel times in the radially anisotropic, spherically symmetric Earth model can be calculated from the equations governing free oscillations of the Earth [*Woodhouse and Girnius*, 1982]. We present an alternative method based on ray theory, which does not require the reference model to be spherically symmetric.

[58] In an anisotropic medium, the propagation velocity of a wavefront varies with the propagation direction. For the transversely isotropic medium with the vertical axis of symmetry, the equation governing the propagation of a plane wave can be solved analytically in terms of three types of body waves with orthogonal polarizations. The wavefronts of the three waves, which are often referred to as *qSH*, *qSV*, and *qP*, propagate with velocities [*Kennett*, 2001]

$$v_{qSH}^{phase} = \sqrt{v_{SV}^2 \cos^2\theta + v_{SH}^2 \sin^2\theta}, \quad v_{qSV}^{phase} = \sqrt{\frac{Z_1 - Z_2}{2}},$$

$$\text{and} \quad v_{qP}^{phase} = \sqrt{\frac{Z_1 + Z_2}{2}}, \tag{A1}$$

where $Z_1 = v_{PV}^2 \cos^2\theta + v_{PH}^2 \sin^2\theta + v_{SV}^2$, $Z_2 = \sqrt{Z_3^2 + Z_4^2}$, $Z_3 = v_{PH}^2 \sin^2\theta - v_{PV}^2 \cos^2\theta + v_{SV}^2 \cos2\theta$, $Z_4 = (\gamma^2 + v_{SV}^2)\sin2\theta$, and θ is the angle of inclination between the vector normal to the wavefront and the vertical axis of symmetry. The

elastic moduli A, C, N, L, F [*Love*, 1927] are often identified with velocities $v_{PH} = \sqrt{\frac{A}{\rho}}$, $v_{PV} = \sqrt{\frac{C}{\rho}}$, $v_{SH} = \sqrt{\frac{N}{\rho}}$, $v_{SV} = \sqrt{\frac{L}{\rho}}$, and with the parameter $\gamma = \sqrt{\frac{F}{\rho}}$. In PREM, the parameter $\eta = \frac{F}{A-2L}$ is defined instead of γ.

[59] The anisotropy causes the energy to propagate along the ray with a different velocity than the phase velocity and the ray to deviate from the direction normal to the wavefront. The angle ϕ^{group} between the ray path and the vertical axis of symmetry is related to the phase velocity and θ by [*Berryman*, 1979; *Thomsen*, 1986]

$$\phi^{group} - \theta = \text{atan}\left(\frac{1}{v^{phase}}\frac{dv^{phase}}{d\theta}\right), \qquad (A2)$$

and the velocity at which the energy propagates along the ray is given by

$$v^{group} = \frac{v^{phase}}{\cos(\phi^{group} - \theta)}. \qquad (A3)$$

We define the linear relationship between the observed travel time anomalies δt and the variations in the elastic parameters as

$$\delta t = -\int_{path} \frac{\delta v^{group}}{(v_0^{group})^2}\, ds, \qquad (A4)$$

where the first-order Taylor series approximation to v^{group} is given by

$$\delta v^{group} = \sum_{i=1}^{5} \frac{\partial v^{group}}{\partial m_i} \delta m_i. \qquad (A5)$$

Here, m_i stands for v_{PH}, v_{PV}, v_{SH}, v_{SV}, and η, and v_0^{group} is the group velocity in the reference model. We determine ray paths using the method of *Woodhouse* [1981]. The partial derivatives and v_0^{group} are evaluated numerically for the reference model from equations (A1)–(A3). Since the integral is taken along the ray path, it does not encounter a singularity at the turning point, which is involved in the formulas of *Woodhouse and Girnius* [1982]. The method presented here, as opposed to that of *Woodhouse and Girnius* [1982], does not require the reference model to be spherically symmetric and therefore can be applied to solve nonlinear inverse problems. This would, however, require tracing rays through a three-dimensional anisotropic model, which is beyond the scope of this paper.

[60] A majority of our teleseismic travel time data are measured on the transverse component of a seismogram, which records qSH waves. Such data are primarily sensitive to the variations in v_{SH} near the turning point in the lower mantle and to the variations in v_{SV} in case of the near vertical propagation. Measurements of the qSV waves, such as SKS or SKKS, recorded on the vertical or longitudinal component, are insensitive to δv_{SH} and very sensitive to δv_{SV} regardless of the propagation direction. Therefore, in order to determine variations in both δv_{SH} and δv_{SV} in the lower mantle, we need to combine the measurements of qSH and qSV waves.

References

Anderson, D. L. (1979), The deep structure of continents, *J. Geophys. Res.*, *84*, 7555–7560.

Anderson, D. L. (1989), *Theory of the Earth*, Blackwell, Oxford, UK.

Bassin, C., G. Laske, and G. Masters (2000), The current limits of resolution for surface wave tomography in North America, *Eos Trans. AGU*, *81*(48), Fall Meet. Suppl., Abstract S12A-03.

Becker, T. W., B. Kustowski, and G. Ekström (2008), Radial seismic anisotropy as a constraint for upper mantle rheology, *Earth Planet. Sci. Lett.*, *267*, 213–227, doi:10.1016/jepsl.2007.11.038.

Beghein, C., J. Trampert, and H. J. van Heijst (2006), Radial anisotropy in seismic reference models of the mantle, *J. Geophys. Res.*, *111*, B02303, doi:10.1029/2005JB003728.

Berryman, J. G. (1979), Long-wave elastic anisotropy in transversely isotropic media, *Geophysics*, *44*, 896–917.

Bolton, H. F., and G. Masters (2001), Travel times of P and S from global digital seismic networks; implications for the relative variation of P and S velocity in the mantle, *J. Geophys. Res.*, *106*, 13,527–13,540.

Boschi, L., and A. M. Dziewonski (1999), High- and low-resolution images of the Earth's mantle: Implications of different approaches to tomographic modeling, *J. Geophys. Res.*, *104*, 25,567–25,594.

Boschi, L., and G. Ekström (2002), New images of the Earth's upper mantle from measurements of surface wave phase velocity anomalies, *J. Geophys. Res.*, *107*(B4), 2059, doi:10.1029/2000JB000059.

Dahlen, F. A., and J. Tromp (1998), *Theoretical Global Seismology*, Princeton Univ. Press, Princeton, N.J.

Durek, J. J., and G. Ekström (1996), A radial model of anelasticity consistent with long-period surface-wave attenuation, *Bull. Seismol. Soc. Am.*, *86*, 144–158.

Dziewonski, A. M. (1971), Upper mantle models from 'pure path' dispersion data, *J. Geophys. Res.*, *76*, 2587–2601.

Dziewonski, A. M. (1984), Mapping the lower mantle; determination of lateral heterogeneity in P velocity up to degree and order 6, *J. Geophys. Res.*, *89*, 5929–5952.

Dziewonski, A. M., and D. L. Anderson (1981), Preliminary reference Earth model, *Phys. Earth Planet. Inter.*, *25*, 297–356.

Dziewonski, A. M., and F. Gilbert (1976), The effect of small, aspherical perturbations on travel times and a re-examination of the corrections for ellipticity, *Geophys. J. R. Astron. Soc.*, *44*, 7–18.

Dziewonski, A. M., and J. H. Woodhouse (1983), An experiment in systematic study of global seismicity: Centroid-moment tensor solutions for 201 moderate and large earthquakes of 1981, *J. Geophys. Res.*, *88*, 3247–3271.

Dziewonski, A. M., and R. L. Woodward (1992), Acoustic imaging at the planetary scale, in *Acoustical Imaging*, vol. 19, edited by H. Emert and H.-P. Harjes, pp. 785–797, Plenum.

Dziewonski, A. M., B. H. Hager, and R. J. O'Connell (1977), Large-scale heterogeneity in the lower mantle, *J. Geophys. Res.*, *82*, 239–255.

Dziewonski, A. M., T.-A. Chou, and J. H. Woodhouse (1981), Determination of earthquake source parameters from waveform data for studies of global and regional seismicity, *J. Geophys. Res.*, *86*, 2825–2852.

Ekström, G. (2000), Mapping the lithosphere and asthenosphere with surface waves: Lateral structure and anisotropy, in *The History and Dynamics of Global Plate Motions*, *Geophys. Monogr. Ser.*, vol. 121, edited by M. A. Richards, R. G. Gordon, and R. D. van der Hilst, pp. 239–255, AGU, Washington, D. C.

Ekström, G., and A. M. Dziewonski (1998), The unique anisotropy of the Pacific upper mantle, *Nature*, *394*, 168–172.

Ekström, G., J. Tromp, and E. W. F. Larson (1997), Measurements and global models of surface wave propagation, *J. Geophys. Res.*, *102*, 8137–8157.

Ekström, G., A. M. Dziewoński, N. N. Maternovskaya, and M. Nettles (2005), Global seismicity of 2003: Centroid-moment tensor solutions for 1087 earthquakes, *Phys. Earth Planet. Inter.*, *148*, 327–351.

Flanagan, M. F., and P. M. Shearer (1998), Global mapping of topography on transition zone velocity discontinuities by stacking SS precursors, *J. Geophys. Res.*, *103*, 2673–2692.

Fukao, Y., S. Widiyantoro, and M. Obayashi (2001), Stagnant slabs in the upper and lower mantle transition region, *Rev. Geophys.*, *39*, 291–323.

Grand, S. P., R. D. van der Hilst, and S. Widiyantoro (1997), Global seismic tomography: A snapshot of convection in the Earth, *GSA Today*, 7, 1–7.

Gu, Y. J., and A. M. Dziewonski (2002), Global variability of transition zone thickness, *J. Geophys. Res.*, 107(B7), 2135, doi:10.1029/2001JB000489.

Gu, Y. J., A. M. Dziewonski, and C. B. Agee (1998), Global de-correlation of the topography of transition zone discontinuities, *Earth Planet. Sci. Lett.*, 157, 57–67.

Gu, Y. J., A. M. Dziewonski, W.-J. Su, and G. Ekström (2001a), Models of the mantle shear velocity and discontinuities in the pattern of lateral heterogeneities, *J. Geophys. Res.*, 106, 11169–11199.

Gu, Y. J., A. M. Dziewonski, and G. Ekström (2001b), Preferential detection of the Lehmann discontinuity beneath continents, *Geophys. Res. Lett.*, 24, 4655–4658.

Gu, Y. J., A. M. Dziewonski, and G. Ekström (2003), Simultaneous inversion for mantle shear velocity and topography of transition zone discontinuities, *Geophys. J. Int.*, 154, 559–583.

Gu, Y. J., A. Lerner-Lam, A. M. Dziewonski, and G. Ekström (2005), Deep structure and seismic anisotropy beneath the East Pacific Rise, *Earth Planet. Sci. Lett.*, 232, 259–272.

Gung, Y., M. Panning, and B. Romanowicz (2003), Global anisotropy and the thickness of continents, *Nature*, 442, 707–711.

Gurnis, M., and B. H. Hager (1988), Controls of the structure of subducted slabs, *Nature*, 335, 317–321.

Hamilton, W. B. (2002), The closed upper-mantle circulation of plate tectonics, in *Plate Boundary Zones, Geodyn. Ser.*, vol. 30, edited by S. Stein and J. T. Freymueller, pp. 359–410, AGU, Washington, D. C.

Helffrich, G. (2000), Topography of the transition zone seismic discontinuities, *Rev. Geophys.*, 38, 141–158.

Jordan, T. H. (1975), The continental tectosphere, *Rev. Geophys. Space Phys.*, 13, 1–12.

Jordan, T. H. (1978), Composition and development of the continental tectosphere, *Nature*, 274, 544–548.

Jordan, T. H. (1981), Continents as a chemical boundary layer, *Phil. Trans. R. Soc. London, Ser. A*, 301, 359–373.

Karato, S. (1993), Importance of anelasticity in the interpretation of seismic tomography, *Geophys. Res. Lett.*, 20, 1623–1626.

Karato, S. (1998), Some remarks on the origin of seismic anisotropy in the D″ layer, *Earth Planet. Sci.*, 50, 1028–1059.

Kendall, J. M. (2000), Seismic anisotropy in boundary layers of the mantle, in *Earth's Deep Interior: Mineral Physics and Tomography From the Atomic to the Global Scale, Geophys. Monogr. Ser.*, vol. 117, edited by S. Karato et al., pp. 133–159, AGU, Washington, D. C.

Kendall, J. M., and P. G. Silver (1996), Constraints from seismic anisotropy on the nature of the lowermost mantle, *Nature*, 381, 409–412.

Kennett, B.L.N. (2001), *The Seismic Wavefield*, vol. 1, Cambridge Univ. Press, Cambridge, UK.

Kennett, B. L. N., E. R. Engdahl, and R. Buland (1995), Constraints on seismic velocities in the Earth from travel times, *Geophys. J. Int.*, 122, 108–124.

Kustowski, B. (2007), Modeling the anisotropic shear-wave velocity structure in the Earth's mantle on global and regional scales, Ph.D. thesis, Harvard Univ., Cambridge, Mass.

Kustowski, B., A. M. Dziewoński, and G. Ekström (2007), Nonlinear crustal corrections for normal-mode seismograms, *Bull Seismol. Soc. Am.*, 97, 1756–1762.

Kustowski, B., et al. (2008), The shear-wave velocity structure in the upper mantle beneath Eurasia, *Geophys. J. Int.*, in press.

Lay, T., and C. J. Young (1990), The stability-stratified outermost core revisited, *Geophys. Res. Lett.*, 17, 2001–2004.

Lay, T., Q. Williams, E. J. Garnero, L. Kellog, and M. E. Wysession (1998), Seismic wave anisotropy in the D″ region and its implications, in *The Core-Mantle Boundary Region, Geodyn. Ser.*, vol. 28, edited by M. Gurnis et al., pp. 219–318, AGU, Washington, D. C.

Li, X.-D., and B. Romanowicz (1995), Comparison of global waveform inversions with and without considering cross-branch modal coupling, *Geophys. J. Int.*, 121, 695–709.

Li, X.-D., and B. Romanowicz (1996), Global mantle shear velocity model developed using nonlinear asymptotic coupling theory, *J. Geophys. Res.*, 101, 22,245–22,272.

Liu, X. (1997), The three-dimensional shear-wave velocity structure of Earth's lowermost mantle, Ph.D. thesis, Harvard Univ., Cambridge, Mass.

Liu, X.-F., and A. M. Dziewonski (1998), Global analysis of shear wave velocity anomalies in the lower-most mantle, in *The Core-Mantle Boundary Layer, Geodyn. Ser.*, vol. 28, edited by M. Gurnis et al., pp. 21–36, AGU, Washington, D. C.

Love, A. E. H. (1927), *A Treatise on the Theory of Elasticity*, 4th ed., Cambridge Univ. Press, Cambridge, UK.

Lundgren, P., and D. Giardini (1994), Isolated deep earthquakes and the fate of subduction in the mantle, *J. Geophys. Res.*, 99, 15,833–15,842.

Marone, F., Y. Gung, and B. Romanowicz (2007), Three-dimensional radial anisotropic structure of the North American upper mantle from inversion of surface waveform data, *Geophys. J. Int.*, 171, 206–222, doi:10.1111/j.1365-246X.2007.03465.

Masters, G., G. Laske, H. Bolton, and A. M. Dziewonski (2000), The relative behavior of shear velocity, bulk sound speed, and compressional velocity in the mantle: Implications for chemical and thermal structure, in *Earth's Deep Interior: Mineral Physics and Tomography From the Atlantic to the Global Scale, Geophys. Monogr. Ser.*, vol. 117, edited by S. Karato et al., pp. 63–87, AGU, Washington, D. C.

Mégnin, C., and B. Romanowicz (2000), The three-dimensional shear velocity structure of the mantle from the inversion of body, surface and higher-mode waveforms, *Geophys. J. Int.*, 143, 709–728.

Menke, W. (1989), *Geophysical Data Analysis: Discrete Inverse Theory*, Academic, San Diego, Calif.

Montagner, J.-P., and D. L. Anderson (1989), Petrological constraints on seismic anisotropy, *Phys. Earth Planet. Inter.*, 54, 82–105.

Montelli, R., G. Nolet, F. A. Dahlen, G. Masters, E. R. Engdahl, and S.-H. Hung (2004a), Finite-frequency tomography reveals a variety of plumes in the mantle, *Science*, 303, 338–343.

Montelli, R., G. Nolet, G. Masters, F. A. Dahlen, and H. S.-Hung (2004b), Global P and PP traveltime tomography: Rays versus waves, *Geophys. J. Int.*, 158, 637–654.

Murakami, M. K., K. Hirose, K. Kawamura, N. Sata, and Y. Ohishi (2004), Post-perovskite phase transition in $MgSiO_3$, *Science*, 304, 855–858.

Nettles, M., and A. M. Dziewoński (2008), Radially anisotropic shear-velocity structure of the upper mantle globally and beneath North America, *J. Geophys. Res.*, 113, B02303, doi:10.1029/2006JB004819.

Nicolas, A., and N. Christensen (1987), Formation of anisotropy in upper mantle peridotites: A review, in *Composition, Structure and Dynamics of the Lithosphere-Asthenosphere System, Geodyn. Ser.*, vol. 16, edited by K. Fuchs and C. Froidevaux, pp. 111–123, AGU, Washington, D. C.

Oganov, A. R., and S. Ono (2004), Theoretical and experimental evidence for a post-perovskite phase of $MgSiO_3$ in the Earth's D″ layer, *Nature*, 430, 445–448.

Panning, M., and B. Romanowicz (2006), A three-dimensional radially anisotropic model of shear velocity in the whole mantle, *Geophys. J. Int.*, 167, 361–379.

Priestley, K., and E. Debayle (2003), Seismic evidence for a moderately thick lithosphere beneath the Siberian Platform, *Geophys. Res. Lett.*, 30(3), 1118, doi:10.1029/2002GL015931.

Ringwood, A. E., and T. Irifune (1988), Nature of the 650-km seismic discontinuity: Implications for mantle dynamics and differentiation, *Nature*, 331, 131–136.

Ritsema, J., and R. M. Allen (2003), The elusive mantle plume, *Earth Planet. Sci. Lett.*, 207, 1–12.

Ritsema, J., J. H.-van Heijst, and J. H. Woodhouse (1999), Complex shear wave velocity structure imaged beneath Africa and Iceland, *Science*, 286, 1925–1928.

Ritsema, J., H.-J. van Heijst, and J. H. Woodhouse (2004), Global transition zone tomography, *J. Geophys. Res.*, 109, B02302, doi:10.1029/2003JB002610.

Robertson, G. S., and J. H. Woodhouse (1996), Ratio of relative S to P velocity heterogeneity in the lower mantle, *J. Geophys. Res.*, 101, 20,041–20,052.

Shapiro, S. S., B. H. Hager, and T. H. Jordan (1999), Stability and dynamics of the continental tectosphere, *Lithos*, 48, 115–133.

Shearer, P. M., and T. G. Masters (1992), Global mapping of topography on the 660-km discontinuity, *Nature*, 355, 791–795.

Shim, S.-H., T. S. Duffy, R. Jeanloz, and G. Shen (2004), Stability and crystal structure of $MgSiO_3$ perovskite to the core-mantle boundary, *Geophys. Res. Lett.*, 31, L10603, doi:10.1029/2004GL019639.

Su, W.-J., and A. M. Dziewonski (1991), Predominance of long-wavelength heterogeneity in the mantle, *Nature*, 352, 121–128.

Su, W.-J., and A. M. Dziewonski (1993), Towards consistent P and S 3-D models of the mantle, *Eos. Trans. AGU*, 74, 16.

Su, W.-J., and A. M. Dziewonski (1997), Simultaneous inversion for 3-D variations in shear and bulk velocity in the mantle, *Phys. Earth Planet. Inter.*, 100, 135–156.

Tackley, P. J., D. J. Stevenson, G. Glatzmaier, and G. Schubert (1993), Effects of an endothermic phase transition at 670 km depth in a spherical model of convection in the Earth's mantle, *Nature*, 361, 699–704.

Takeuchi, H., and M. Saito (1972), Seismic surface waves, in *Seismology: Surface Waves and Earth Oscillations, Methods in Comput. Phys.*, vol. 11, edited by B. A. Bolt, pp. 217–295, Academic, New York.

Thomsen, L. (1986), Weak elastic anisotropy, *Geophysics*, 51, 1954–1966.

Trampert, J., and J. Spetzler (2006), Surface wave tomography; finite-frequency effects lost in the null space, *Geophys. J. Int.*, 164, 394–400.

Trefethen, L. N., and D. Bau (1997), *Numerical Linear Algebra*, Soc. for Ind. and Appl. Math., Philadelphia, Pa.

van der Hilst, R. D., and M. V. de Hoop (2005), Banana-doughnut kernels and mantle tomography, *Geophys. J. Int.*, *163*, 956–961.

van der Hilst, R. D., S. Widiyantoro, and E. R. Engdahl (1997), Evidence for deep mantle circulation from global tomography, *Nature*, *386*, 578–584.

Vinnik, L. P., V. Farra, and B. Romanowicz (1989), Observational evidence for diffracted SV in the shadow of the Earth's core, *Geophys. Res. Lett.*, *16*, 519–522.

Wang, Z., and F. A. Dahlen (1995), Spherical-spline parameterization of three-dimensional Earth models, *Geophys. Res. Lett.*, *22*, 3099–3102.

Woodhouse, J. H. (1981), A note on the calculation of travel times in a transversely isotropic Earth model, *Phys. Earth Planet. Inter.*, *25*, 357–359.

Woodhouse, J. H., and A. M. Dziewonski (1984), Mapping the upper mantle: Three-dimensional modeling of Earth structure by inversion of seismic waveforms, *J. Geophys. Res.*, *89*, 5953–5986.

Woodhouse, J. H., and T. P. Girnius (1982), The calculation of $d\Delta/dp$ and of partial derivatives for travel-time inversion in transversely isotropic spherical earth models, in *Seismic Discrimination, Semiannual Technical Summary Report to the Defense Advanced Research Projects Agency*, pp. 61–65, Mass. Inst. of Technol. Lincoln Lab., Lexington, Mass.

Woodward, R. L., and G. Masters (1991), Global upper mantle structure from long-period differential travel-times, *J. Geophys. Res.*, *96*, 6351–6377.

Zhou, Y., G. Nolet, F. A. Dahlen, and G. Laske (2006), Global upper-mantle structure from finite-frequency surface-wave tomography, *J. Geophys. Res.*, *111*, B04304, doi:10.1029/2005JB003677.

————————————

A. M. Dziewoński, Department of Earth and Planetary Sciences, Harvard University, 20 Oxford Street, Cambridge, MA 02138, USA.

G. Ekström, Lamont-Doherty Earth Observatory, Columbia University, 61 Route 9W, Palisades, NY 10964, USA. (ekstrom@ldeo.columbia.edu)

B. Kustowski, Chevron, 6001 Bollinger Canyon Road, D1136, San Ramon, CA 94583, USA. (kustowski@post.harvard.edu)